

www.acsami.org Research Article

# Large Thermo-Spin Effects in Heusler Alloy-Based Spin Gapless Semiconductor Thin Films

Amit Chanda,\* Deepika Rani, Derick DeTellem, Noha Alzahrani, Dario A. Arena, Sarath Witanachchi, Ratnamala Chatterjee, Manh-Huong Phan, and Hariharan Srikanth\*



Cite This: ACS Appl. Mater. Interfaces 2023, 15, 53697–53713



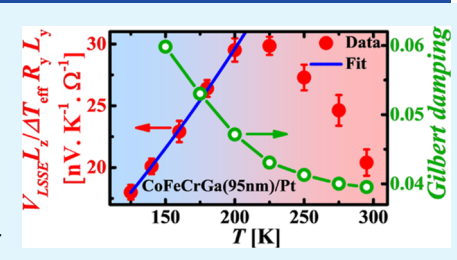
**ACCESS** I

III Metrics & More

Article Recommendations

s Supporting Information

**ABSTRACT:** Recently, Heusler alloy-based spin gapless semiconductors (SGSs) with high Curie temperature ( $T_{\rm C}$ ) and sizable spin polarization have emerged as potential candidates for tunable spintronic applications. We report comprehensive investigation of the temperature-dependent ANE and intrinsic longitudinal spin Seebeck effect (LSSE) in CoFeCrGa thin films grown on MgO substrates. Our findings show that the anomalous Nernst coefficient for the MgO/CoFeCrGa (95 nm) film is  $\approx$ 1.86  $\mu$ V K<sup>-1</sup> at room temperature, which is nearly 2 orders of magnitude higher than that of the bulk polycrystalline sample of CoFeCrGa ( $\approx$ 0.018  $\mu$ V K<sup>-1</sup>) and almost 3 orders of magnitude higher than that of the half-metallic ferromagnet La<sub>1-x</sub>Na<sub>x</sub>MnO<sub>3</sub> ( $\approx$ 0.005  $\mu$ V



 $K^{-1}$ ) but comparable to that of the magnetic Weyl semimetal  $Co_2MnGa$  thin film ( $\approx 2-3~\mu V~K^{-1}$ ). Furthermore, the LSSE coefficient for our MgO/CoFeCrGa (95 nm)/Pt (5 nm) heterostructure is  $\approx 20.5~nV~K^{-1}~\Omega^{-1}$  at room temperature, which is twice larger than that of the half-metallic ferromagnetic  $La_{0.7}Sr_{0.3}MnO_3$  thin films ( $\approx 9~nV~K^{-1}~\Omega^{-1}$ ). We show that both ANE and LSSE coefficients follow identical temperature dependences and exhibit a maximum at  $\approx 225~K$ , which is understood as the combined effects of inelastic magnon scatterings and reduced magnon population at low temperatures. Our analyses not only indicate that the extrinsic skew scattering is the dominating mechanism for ANE in these films but also provide critical insights into the functional form of the observed temperature-dependent LSSE at low temperatures. Furthermore, by employing radio frequency transverse susceptibility and broad-band ferromagnetic resonance in combination with the LSSE measurements, we establish a correlation among the observed LSSE signal, magnetic anisotropy, and Gilbert damping of the CoFeCrGa thin films, which will be beneficial for fabricating tunable and highly efficient Heusler alloy-based spin caloritronic nanodevices.

KEYWORDS: longitudinal spin Seebeck effect, anomalous Nernst effect, spin gapless semiconductor, Heusler alloy, magnetic anisotropy, Gilbert damping

### 1. INTRODUCTION

The past few years have witnessed extensive research efforts in the field of spin caloritronics for the development of highly efficient next-generation spin-based electronic devices by combining the versatile advantages of spintronics and thermoelectricity, with the aim of finding novel avenues for waste heat recovery and thermoelectric energy conversion. Fundamental knowledge of the interplay between heat, charge, and spin degrees of freedom not only allowed us to understand how thermal gradients can be utilized to manipulate and control the flow of spin angular momenta inside a material at the nanoscale but also helped the scientific community to explore various intriguing thermo-spin transport phenomena, such as the anomalous Nernst effect (ANE), spin Seebeck effect, spin Peltier effect, and so on.

The ANE refers to the generation of a transverse thermoelectric voltage in a magnetic conductor/semiconductor by the application of a thermal gradient and an external magnetic field.<sup>5</sup> The ANE has been observed in a large range of magnetic materials, from half-metallic ferromagnets such as hole-doped manganites,<sup>6</sup> cobaltites,<sup>7</sup> and spin gapless semi-

conductors<sup>8</sup> to ferrimagnets such as iron oxide,<sup>9</sup> as well as unconventional magnetic systems with topologically nontrivial phases such as topological full Heusler ferromagnets,<sup>10</sup> ferromagnetic Weyl semimetals,<sup>11,12</sup> etc. In a topological magnetic material, charge carriers moving through a periodic potential with strong spin—orbit coupling (SOC) acquire an additional anomalous velocity perpendicular to their original trajectory due to the nonzero Berry curvature at the Fermi level.<sup>13</sup> This anomalous velocity causes a real space spin selective deflection of the charge carriers and leads to a potentially large ANE response in these topological magnetic materials compared to conventional magnets.<sup>13</sup> In addition to the aforementioned intrinsic origin, ANE can also originate from extrinsic effects, for example, asymmetric skew scattering

Received: August 18, 2023 Revised: October 23, 2023 Accepted: October 26, 2023 Published: November 8, 2023





of charge carriers as observed in Heusler ferromagnets, 14 holedoped manganites, cobaltites, spin gapless semiconductors, iron oxide, etc.

On the other hand, the longitudinal spin Seebeck effect (LSSE) refers to the thermal generation of magnonic spin current in a ferromagnetic (FM) material by the concurrent applications of a temperature gradient and an external magnetic field across a FM/heavy metal (HM) bilayer structure and injection of that spin current to the adjacent HM layer with strong SOC, which is then converted into electrically detectable charge current in the HM layer via the inverse spin Hall effect (ISHE). 1,3,15 The bilayer structure consists of the ferrimagnetic insulator Y<sub>3</sub>Fe<sub>5</sub>O<sub>12</sub> (YIG), and Pt is known as the benchmark system for generating pure spin current and hence LSSE. 3,16-18 Apart from YIG, other magnetic insulators, for example, the compensated ferrimagnetic insulator  $Gd_3Fe_5O_{12}$ , <sup>15</sup> the noncollinear antiferromagnetic insulator  $LuFeO_3$ , <sup>19</sup> etc., have also emerged as promising spin caloritronic materials. Nevertheless, observation of LSSE is not only restricted to magnetic insulators, but it has also been observed in metallic, 20 half-metallic, 21-23 and semiconducting ferromagnets.<sup>24</sup>

Although ANE and LSSE are two distinct types of magnetothermoelectric phenomena, they share common origin for materials exhibiting extrinsic effect-dominated ANE.<sup>25</sup> In both the cases, simultaneous application of thermal gradient and external magnetic field generates magnonic excitations. While in the case of ANE, the thermally generated magnons transfer spin angular momenta to the itinerant electrons of the FM via the electron-magnon scattering and thereby dynamically spin polarizes them, in the case of LSSE, a spatial gradient of those thermally generated magnons leads to magnon accumulation close to the FM/HM interface and pumps spin current to the HM layer.<sup>25</sup> Large magnon-induced ANE has been observed in MnBi single crystal.<sup>25</sup> However, observation of large ANE in a FM conductor does not necessarily indicate a promise for a large LSSE and vice versa. Therefore, it would be technologically advantageous from the perspective of spin caloritronic device applications and thermal energy harnessing to search for a FM material that can simultaneously exhibit large LSSE and ANE.

In recent years, Heusler alloy-based spin gapless semiconductors (SGSs) have emerged as promising magnetic materials for tunable spintronic applications as they not only combine the characteristics of both half-metallic ferromagnets and gapless semiconductors but also possess high Curie temperature  $(T_{\rm C})$  and substantial spin polarization. We have recently observed large ANE in the bulk sample of Heusler alloy-based SGS/CoFeCrGa with  $T_C \approx 690 \text{ K},^{8,27,28}$ which was the first experimental observation of ANE in the SGS family. Our fascinating observation motivated us to explore ANE as well as LSSE in the CoFeCrGa thin films. Although SGS has been theoretically predicted to be a promising candidate for spintronic applications, <sup>29</sup> there is no previous experimental study on the thermo-spin transport phenomena, especially LSSE in SGS thin films. In this paper, we report on the temperature-dependent ANE and LSSE in the CoFeCrGa single layer and CoFeCrGa/Pt bilayer films with different CoFeCrGa film thicknesses. We found that both ANE and LSSE coefficients follow identical temperature dependences and exhibit a maximum at ≈225 K, which is understood as the combined effects of inelastic magnon scatterings and reduced magnon population at low temperatures. Our analyses

not only indicate that the extrinsic skew scattering is the dominating mechanism for ANE in these films but also provide critical insights into the functional form of the observed temperature-dependent LSSE. Furthermore, we have established a correlation among the observed LSSE signal, magnetic anisotropy, and Gilbert damping of the CoFeCrGa thin films, which will be beneficial for fabricating tunable and efficient spin caloritronic devices.

# 2. EXPERIMENTAL SECTION

The thin films of CoFeCrGa were grown on single-crystal MgO (001) substrates of surface area 5 × 5 mm<sup>2</sup> using an excimer KrF pulsed laser deposition (PLD) system. The films were deposited at 500 °C and were further annealed in situ at 500 °C for 30 min to further enhance the chemical order and crystallization. The film surface morphology was investigated by field emission gun-scanning electron microscopy (FEG-SEM) and atomic force microscopy (AFM), while the structural properties of the thin films were identified by X-ray diffraction (XRD) using monochromatic Cu K $\alpha$  radiation.

AFM and temperature-dependent magnetic force microscopy (MFM) measurements were performed on a Hitachi 5300E system. All measurements were done under high vacuum ( $P \le 10^{-6}$  Torr). MFM measurements utilized PPP-MFMR tips, which were magnetized out of plane with respect to the tip surface via a permanent magnet. Films were first magnetized to their saturation magnetization by being placed in a 1 T static magnetic field, in plane with the film surface. After that AC demagnetization of the film was implemented before initiating the MFM scans. After scans were performed, first a linear background was subtracted which comes from the film not being completely flat on the sample stage. After that, a parabolic background was subtracted, which arises from the nonlinear motion of the piezoelectric crystal that drives the x-y translation. Phase standard deviation was determined by fitting a Gaussian to the image phase distribution and extracting the standard deviation from the fit parameters.

The DC magnetic measurements on the samples at temperatures between 100 and 300 K were performed using a vibrating sample magnetometer (VSM) attached to a physical property measurement system (PPMS), Quantum Design. A linear background originating from the diamagnetic MgO substrate was thereby subtracted. Due to a trapped remanent field inside the superconducting coils, the measured magnetic field was corrected using a paramagnetic reference sample.

The longitudinal electrical resistivity, longitudinal Seebeck coefficient, and thermal conductivity of the bulk samples were simultaneously measured with the thermal transport option (TTO) of the PPMS. The electrical resistivity, magnetoresistance, and Hall measurements on the thin-film samples were performed using the DC resistivity option of the PPMS by employing a standard four-point measurement technique with sourcing currents of 500  $\mu$ A and 1 mA, respectively.

The temperature dependence of the effective magnetic anisotropy fields of the MgO/CoFeCrGa films were measured by using a radio frequency (RF) transverse susceptibility (TS) measurement technique that exploits a self-resonant tunnel diode oscillator (TDO) circuit with a resonance frequency of  $\approx$ 12 MHz.<sup>30</sup> The PPMS was used as a platform to sweep the external DC magnetic field and temperature. During the TS measurement, the MgO/CoFeCrGa thin-film samples were firmly placed inside an inductor coil (L), which is a component of an LC resonator circuit. The coil containing the sample was positioned at the base of the PPMS sample chamber through a multifunctional PPMS probe in such a way that the axial RF magnetic field generated inside the coil stayed parallel to the film surface but perpendicular to the DC magnetic field generated by the superconducting magnet of the PPMS. In the presence of both the RF and DC magnetic fields, the dynamic transverse susceptibility of the sample changes, which eventually changes the resonance frequency of the LC circuit. From the magnetic field dependence of the shift in the resonance frequency recorded by an Agilent frequency counter, we obtained the field-dependent transverse susceptibility.

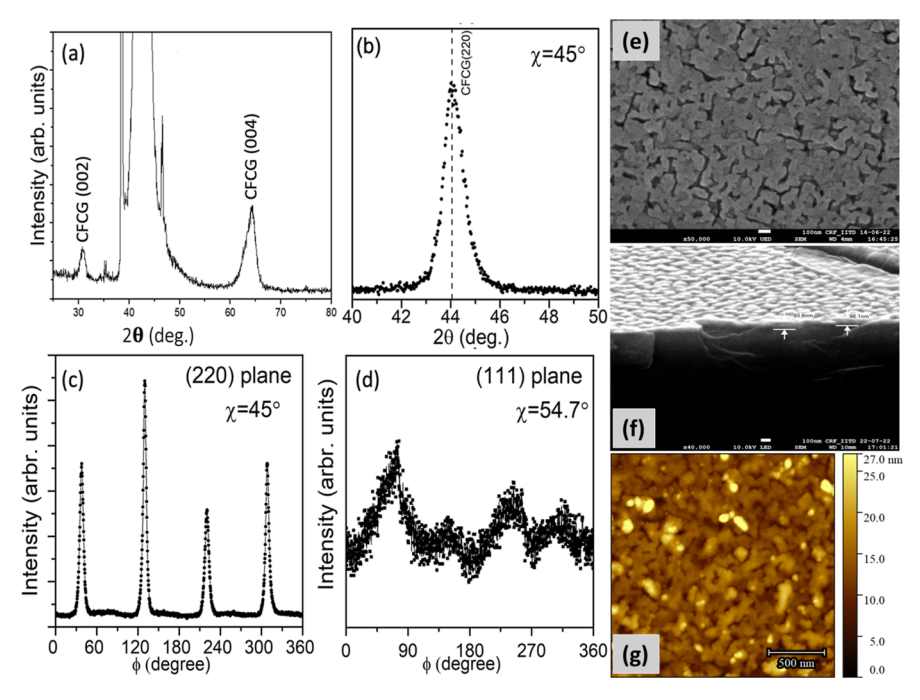


Figure 1. (a) XRD of the MgO/CoFeCrGa (95 nm) film:  $\omega$ -2 $\theta$  (out-of-plane) scan. (b)  $2\theta$ - $\theta$  scan of the (022) plane. (c) Phi-scan of the (022) plane. (d)  $\phi$ -scan of the (111) plane. (e) FEG-SEM, (f) cross-sectional SEM image, and (g) AFM image for the MgO/CoFeCrGa (95 nm) film.

The ANE and LSSE measurements were performed using a custom-designed setup assembled on a universal PPMS sample puck, as shown in our previous reports. 8,31 For both the measurements, the thin-film samples were sandwiched between two copper plates. A single layer of thin Kapton tape was thermally anchored to the bare surfaces of the top (cold) and bottom (hot) copper plates. Cryogenic Apiezon N-grease was used to create good thermal connectivity between the thin-film surface and that of the Kapton tapes. A resistive heater (PT-100 RTD sensor) and a calibrated Si-diode thermometer (DT-621-HR silicon diode sensor) were attached to each of those copper plates. The temperatures of both these copper plates were monitored and controlled individually by employing two distinct separate temperature controllers (Scientific Instruments Model no. 9700). The top copper plate was thermally linked to the base of the PPMS universal puck using a pair of molybdenum screws, and a 4 mm-thick Teflon block was thermally sandwiched between the universal PPMS puck base and the bottom copper plate to maintain a temperature difference of ~10 K between the hot copper plate and the PPMS universal puck base. The Ohmic contacts for the ANE and LSSE voltage measurements were made by using a pair of thin gold wires of 25  $\mu$ m diameter to the Pt layer by high-quality conducting silver paint (SPI Supplies). In the presence of an applied temperature gradient along the z-direction, and an in-plane external DC magnetic field applied along the x-direction, the transverse thermoelectric voltage generated along the y-direction across the Pt layer due to the ISHE  $(V_{\text{ISHE}})$  and across the CoFeCrGa film itself due to the ANE was recorded with a Keithley 2182a nanovoltmeter.

Broad-band ferromagnetic resonance (FMR) measurements were performed using a broad-band FMR spectrometer (NanOsc Phase-FMR, Quantum Design Inc., USA) integrated to the Dynacool PPMS.

# 3. RESULTS AND DISCUSSION

**3.1. Structural and Morphological Properties.** Figure 1a shows the X-ray  $2\theta-\omega$  (out of plane) diffraction pattern for the CoFeCrGa (95 nm) film grown on the MgO (001) substrate. In addition to the peaks corresponding to the MgO substrate, there are additional (002) and (004) diffraction peaks from the film, indicating the growth in the (001) orientation. The formation of a B2 CoFeCrGa structure is

confirmed by the presence of the (002) peak. To find the CoFeCrGa (220) peak intensity, a  $2\theta-\theta$  scan was performed with  $\chi=45^{\circ}$  as shown in Figure 1b. The lattice parameter as estimated by applying the Bragg equation to the (022) peak was found to be 5.76 Å.

It is known that the quaternary Heusler alloys with the composition  $X_1X_2YZ$  exhibit a LiMgPdSn-type (Y-type) cubic structure, wherein the four constituent atoms occupy different Wyckoff positions at 4a (0,0,0), 4b (1/2,1/2,1/2), 4c (1/4,1/ 4.1/4), and 4d (3/4.3/4.3/4). Depending on the occupation of the aforementioned Wyckoff positions by different constituent atoms, there exists three different types (type I, type II, and type III) of configurations.<sup>32</sup> It is interesting to note that exchanging atoms between the 4a and 4b sites or 4c and 4d sites as well as between the groups  $(4a, 4b) \leftrightarrow (4c, 4d)$ does not change the structure.<sup>32</sup> The most stable structural configuration can only be determined with the help of density functional theory. From the first-principles electronic structure calculations, it was previously reported by different groups that the type I configuration with Co at 4a, Fe at 4b, Cr at 4c, and Ga at 4d is the most energetically stable structure for both the bulk and thin film of CoFeCrGa. 27,28,33

To further confirm the epitaxial growth of the CoFeCrGa (95 nm) film,  $\phi$ -scan was performed for the (220) and (111) planes by tilting the sample, i.e.,  $\chi = 45^{\circ}$  for the (220) plane and  $\chi = 54.7^{\circ}$  for the (111) plane (Figure 1c,d). The  $\phi$ -scans of both (220) and (111) planes show a 4-fold symmetry, as four well-defined peaks periodically separated from each other by 90° were observed. The presence of both (111) and (200) peaks rule out the possibility of complete A2 or B2 disorder; however, partial disorder can still be present. The chemical composition was interpreted by the scanning electron microscopy energy-dispersive spectroscopy (SEM-EDS) measurements and was found to be Co<sub>1.05</sub>Fe<sub>1.05</sub>Cr<sub>0.9</sub>Ga<sub>0.99</sub>, which is very close to the ideal stoichiometric composition expected for an equiatomic quaternary Heusler alloy. The surface morphology of the film obtained from the FEG-SEM image

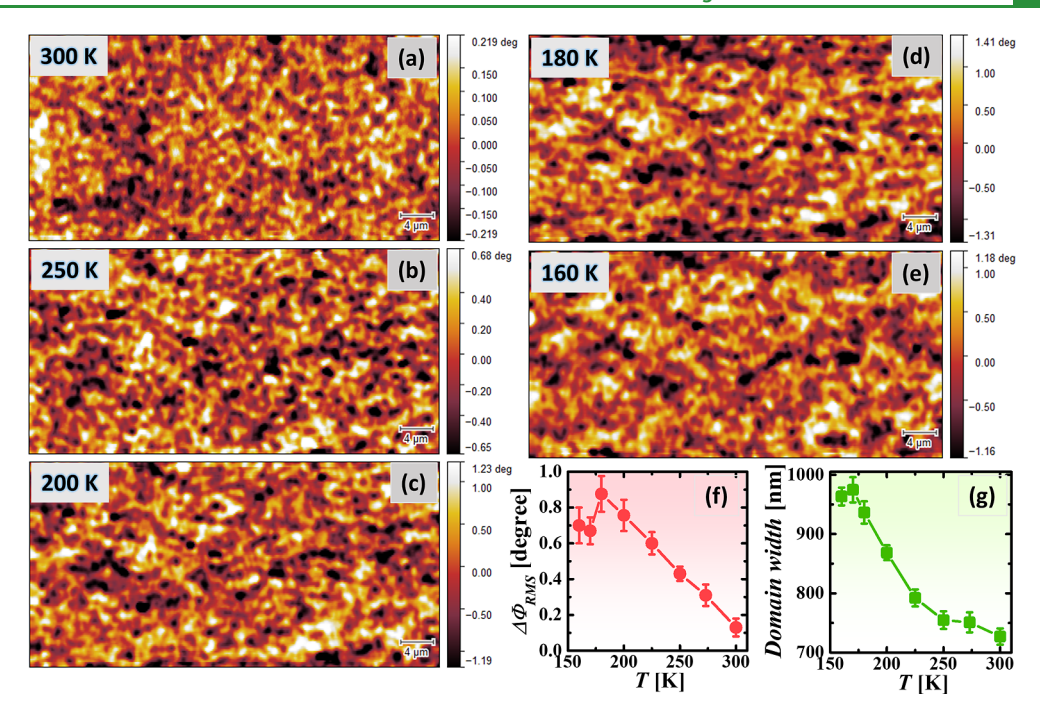


Figure 2. Magnetic force microscopy (MFM) images of the MgO/CoFeCrGa (95 nm) film measured at (a) T=300 K, (b) T=250 K, (c) T=200 K, (d) T=180 K, and (e) T=160 K while cooling the sample after applying an IP magnetic field (higher than the IP saturation field) and then AC demagnetization of the sample at 300 K. (f) rms value of the phase shift,  $\Delta\phi_{\rm rms}$  as a function of temperature for the MgO/CoFeCrGa (95 nm) film extracted from the MFM images. (g) Average domain width as a function of temperature obtained from the MFM images.

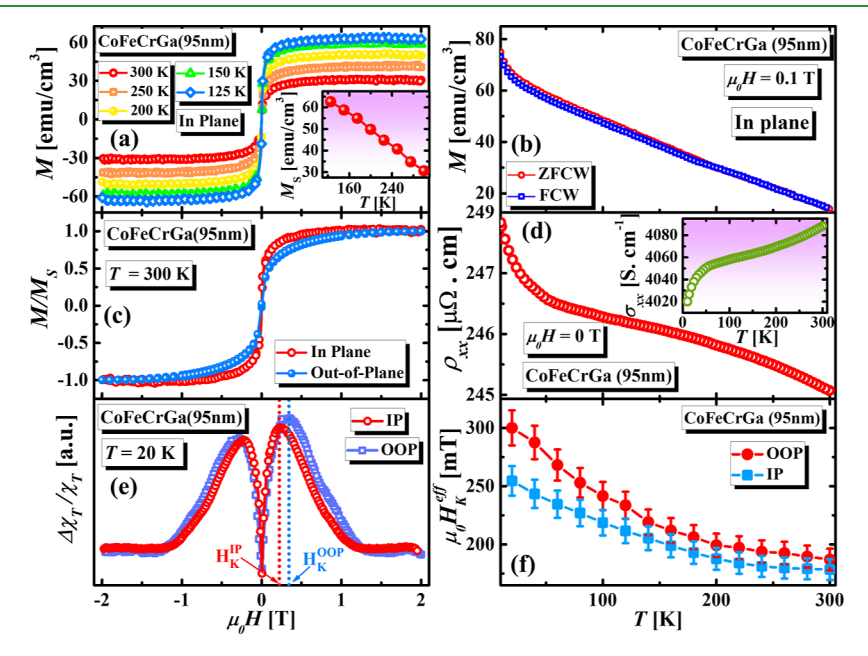


Figure 3. (a) Main panel: magnetic field dependence of magnetization, M(H) of our MgO/CoFeCrGa (95 nm) film measured at selected temperatures in the range 125 K  $\leq T \leq$  300 K in the presence of an in-plane sweeping magnetic field, inset: temperature dependence of the saturation magnetization,  $M_S$ . (b) Temperature dependence of magnetization, M(T), measured in zero-field-cooled warming (ZFCW) and field-cooled-warming (FCW) protocols in the presence of an external magnetic field:  $\mu_0 H = 0.1$  T. (c) Normalized M(H) hysteresis loops at T = 300 K for the in-plane (IP) and out-of-plane (OOP) configurations. (d) Main panel: temperature dependence of longitudinal resistivity,  $\rho_{xx}(T)$ , for the MgO/CoFeCrGa film in the temperature range 10 K  $\leq T \leq 300$  K, the inset shows the corresponding temperature dependence of electrical conductivity,  $\sigma_{xx}(T)$ . (e) Bipolar field scans  $(+H_{DC}^{max} \rightarrow -H_{DC}^{max} \rightarrow +H_{DC}^{max})$  of  $\frac{\Delta \chi_T}{\chi_T}(H_{DC})$  for the MgO/CoFeCrGa (95 nm) film measured at T = 20 K for both IP  $(H_{DC})$  is parallel to the film surface) and OOP  $(H_{DC})$  is perpendicular to the film surface) configurations. (f) Temperature variations of the effective anisotropy fields:  $H_K^{IP}$  and  $H_K^{OOP}$  for our MgO/CoFeCrGa (95 nm) film.

is shown in Figure 1e, which indicates that the film is homogeneous, which was further confirmed by AFM measurements as shown in Figure 1g. A low root-mean-square (rms)

roughness of  $\approx$ 2.5.5 nm is achieved for the CoFeCrGa film, as noticeable in the AFM image shown in Figure 1g. The cross-

sectional SEM image of the film is shown in Figure 1f, which indicates that the film thickness is  $\approx 95 \pm 5$  nm.

In Figure 2, we show the temperature-dependent magnetic force microscopy (MFM) images recorded on the MgO/ CoFeCrGa (95 nm) film. The MFM image at 300 K (see Figure 2a) shows a bright/dark contrast with highly irregularshaped features, indicating cloudlike domain clusters. Note that in MFM, the domain-image contrast is determined by the magnetic force gradient  $\left(\frac{dF}{dz}\right)$  between the sample and the MFM tip (magnetized  $\perp$  to the film surface), which is proportional to the perpendicular component of the stray field of the film.<sup>34</sup> For our film, due to the low bright/dark contrast patterns of the MFM images in the *T*-range, 160 K  $\leq T \leq$  300 K (Figure 2a-e), the domain boundaries are not very well defined. A steep increase in the root-mean-square (rms) value of the phase shift,  $^{34}$   $\Delta\phi_{\rm rms} \approx {Q\over K} \left[{{\rm d}F\over{\rm d}z}\right]$  ( Q= quality factor and K=spring constant of the tip; hence,  $\Delta\phi_{
m rms} \propto$  average domain contrast) has also been observed below 300 K (see Figure 2f). However,  $\Delta\phi_{\rm rms}$  decreases slightly below 180 K. Average domain widths were determined by calculating the 2D autocorrelation across the MFM images, then determining the full-width half-max (fwhm) of arbitrary lines through the 2D autocorrelation spectra. As shown in Figure 2g, the average domain width also increases with decreasing temperature, followed by a slight decrease below 170 K.

3.2. Magnetic and Electrical Transport Properties. Previous studies on bulk CoFeCrGa<sup>27,28</sup> as well as MgO/ CoFeCrGa thin films<sup>35</sup> reveal that the ferromagnetic transition temperature of this sample is very high (at least  $\geq 500$  K). The main panel of Figure 3a shows the magnetic field dependence of magnetization, M(H) of our MgO/CoFeCrGa film measured at selected temperatures in the range 125 K  $\leq T$ ≤ 300 K in the presence of an in-plane sweeping magnetic field. The M(H) loops exhibit very small coercivity throughout the measured temperature range. As shown in the inset of Figure 3a, the saturation magnetization,  $M_S$ , increases almost linearly with decreasing temperature, which is in agreement with the temperature-dependent  $\Delta\phi_{\rm rms}$  obtained from the MFM images. In Figure 3b, we show the temperature dependence of magnetization, M(T), measured in zero-fieldcooled warming (ZFCW) and field-cooled-warming (FCW) protocols in the presence of an external magnetic field:  $\mu_0 H =$ 0.1 T. It is evident that both ZFCW and FCW M(T) increase with decreasing temperature down to 10 K below which it shows a slight up-turn. Furthermore, the ZFCW and FCW M(T) curves do not exhibit any considerable bifurcation at low temperatures, which is indicative of the absence of any glassy magnetic ground state. Figure 3c shows the normalized M(H)hysteresis loops at T = 300 K for the in-plane (IP) and out-ofplane (OOP) configurations, confirming the soft ferromagnetic nature of the film along the IP direction, which is consistent with a recent report on this system.<sup>38</sup>

The main panel of Figure 3d demonstrates the T-dependence of longitudinal resistivity,  $\rho_{xx}(T)$ , for the MgO/CoFeCrGa (95 nm) film in the temperature range 10 K  $\leq T \leq$  300 K. It is obvious that  $\rho_{xx}(T)$  exhibits semiconducting-like resistivity  $\left(\frac{\partial \rho_{xx}}{\partial T} > 0\right)$  throughout the temperature range. The inset of Figure 3d shows the T-dependence of electrical conductivity,  $\sigma_{xx}(T)$ , for the MgO/CoFeCrGa film. Note that the values of both  $\rho_{xx}(T)$  and  $\sigma_{xx}(T)$  for our MgO/CoFeCrGa

film are quite close to those reported on the same film with 12 nm thickness. The furthermore, the linear temperature coefficient of the resistivity for our MgO/CoFeCrGa (95 nm) film was found to be  $\approx -1.37 \times 10^{-10}~\Omega$  m/K, which is of the same magnitude to that reported for different Heusler alloy-based spin gapless semiconductors (SGSs), such as Mn<sub>2</sub>CoAl (-1.4  $\times~10^{-9}~\Omega$ m/K), CoFeMnSi (-7  $\times~10^{-10}~\Omega$ m/K), CoFeCrAl (-5  $\times~10^{-9}~\Omega$ m/K), and CoFeCrGa (-1.9  $\times~10^{-9}~\Omega$ m/K)) thin films.

It is known that the SGS-based Heusler materials are extremely susceptible to disorder, which causes significant changes in the electronic transport properties. Although it is evident from the XRD measurements that both (111) and (200) diffraction peaks are present in our MgO/CoFeCrGa (95 nm) film that rules out the possibility of complete A2 or B2 disorder, it is plausible that partial disorder and defects (antistite disorders, vacancies, etc.) are present in our film.  $^{33,37-39}$  We have performed  $\rho_{xx}(T)$  measurements on two additional MgO/CoFeCrGa films with 200 and 50 nm thicknesses, as shown in the Supporting Information (Figure S3). Although both MgO/CoFeCrGa (200 nm) and MgO/ CoFeCrGa (50 nm) films exhibit negative temperature coefficient similar to the MgO/CoFeCrGa (95 nm) film at low temperatures, they show distinct temperature dependence. While the behavior of  $\rho_{xx}(T)$  for our MgO/CoFeCrGa (200 nm) film resembles that for the SGS CoFeMnSi thin film, <sup>40</sup> the same for MgO/CoFeCrGa (50 nm) film follows the trend of the SGS CoFeCrAl ribbon.<sup>37</sup> Furthermore,  $\rho_{xx}(T)$  for the MgO/CoFeCrGa (200 nm) film exhibits a clear sign change of slope around 200 K, whereas that for MgO/CoFeCrGa (95 nm) and MgO/CoFeCrGa (50 nm) films does not show any sign change of slope in the respective  $\rho_{xx}(T)$  curves.

Notably, the  $\rho_{xx}(T)$  data for MgO/CoFeCrGa (95 nm) only shows a slope change below 50 K, whereas that for the MgO/CoFeCrGa (50 nm) film does not show any slope change in the measured temperature regime. Sign change of slope in the  $\rho_{xx}(T)$  curve has been observed in the SGS Mn<sub>2</sub>CoAl-oriented film grown on the GaAs substrate, <sup>41</sup> which arises from atomic disorder and defects in the films. <sup>42</sup> On the contrary, the  $\rho_{xx}(T)$  data for the Mn<sub>2</sub>CoAl-oriented films grown on thermally oxidized Si substrate only shows a slope change, <sup>42</sup> similar to our MgO/CoFeCrGa (95 nm) film. These observations indicate that our MgO/CoFeCrGa films possess partial disorder/defects that gives rise to the slight difference in the temperature-dependent electronic transport properties in the films with different thicknesses, and the degree of disorder/defect increases with increasing film thickness.

To understand the impact of the atomic disorder and defects in our MgO/CoFeCrGa films further, we have performed isothermal magnetic field-dependent longitudinal resistivity ( $\rho_{xx}$ ) measurements on the MgO/CoFeCrGa (95 nm) film in the presence of an external DC magnetic field applied perpendicular to the film surface. We define the magneto-

resistance (MR) as MR<sub>xx</sub>(%) = 
$$\left[\frac{\rho_{xx}(\mu_0 H) - \rho_{xx}(\mu_0 H = 0)}{\rho_{xx}(\mu_0 H = 0)}\right] \times 100\%$$
,

where  $\rho_{xx}(\mu_0 H=0)$  represents the resistivity at zero applied magnetic field. The magnetic field dependence of magnetoresistance,  $MR_{xx}(H)$ , for the MgO/CoFeCrGa (95 nm) film recorded at selected temperatures in the range  $10 \text{ K} \leq T \leq 300 \text{ K}$  is shown in Figure 4a. Evidently, the MgO/CoFeCrGa (95 nm) film shows negative  $MR_{xx}$  throughout the measured temperature range without any sign change,  $^{26}$  similar to the other SGS materials.  $^{33,35,41,42}$  Additionally,  $MR_{xx}(H)$  is

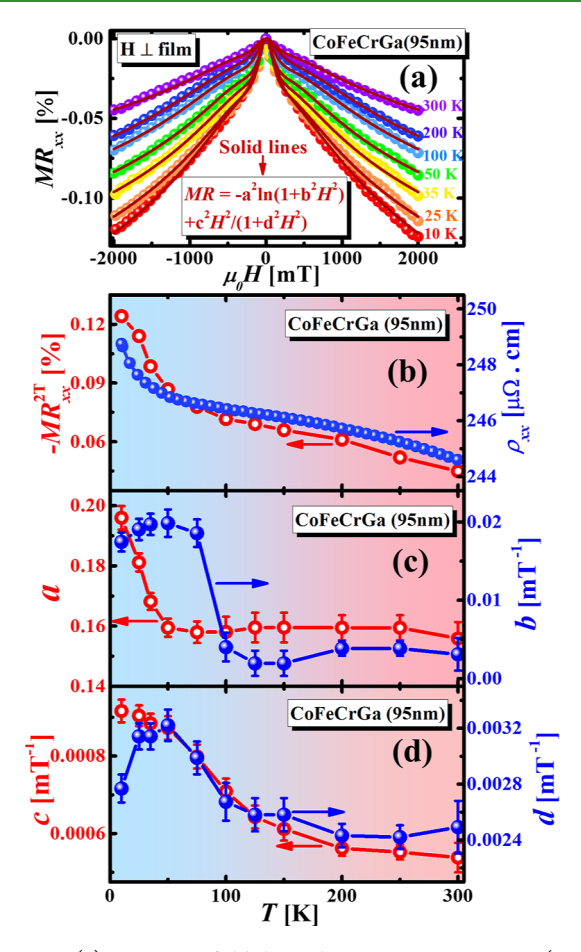


Figure 4. (a) Magnetic field-dependent magnetoresistance (MR<sub>xx</sub>) defined as MR<sub>xx</sub>(%) =  $\left[\frac{\rho_{xx}(\mu_0 H) - \rho_{xx}(\mu_0 H = 0)}{\rho_{xx}(\mu_0 H = 0)}\right] \times 100\%$  for the MgO/CoFeCrGa (95 nm) film at selected temperatures, (b) temperature dependence of MR<sub>xx</sub> on the left *y*-scale, and  $\rho_{xx}(T)$  is shown on the right *y*-scale, temperature dependence of the fitting parameters, *a* and *b* are shown in (c), and that of *c* and *d* are shown in (d).

nonsaturating even at the  $\mu_0 H = 2$  T magnetic field and shows nearly linear behavior in the high field region. These specific features are signature of SGS materials. The left y-scale of Figure 4b demonstrates the temperature dependence of  $-MR_{xx}$  ( $\mu_0H=2$  T) which clearly follows the  $\rho_{xx}$  behavior of this sample. In other words,  $|MR_{xx}(\mu_0 H = 2 \text{ T})|$  increases with decreasing temperature and shows a slope-change around 50 K, below which it increases rapidly. However, the temperature dependence of  $|MR_{xx}(\mu_0 H = 2 T)|$  does not show any low temperature maximum, followed by a dramatic decrease as observed in oriented Mn<sub>2</sub>CoAl films. 41,42 As shown in Figure S7,  $|MR_{xx}(\mu_0 H)|$  for both MgO/CoFeCrGa (50 nm) and MgO/CoFeCrGa (200 nm) films increases with decreasing temperature, indicating the absence of any lowtemperature maximum or drop in  $|MR_{xx}(\mu_0 H)|$  at low temperatures. MRxx in SGS materials is believed to be originated from the spin-dependent scattering, which increases at low temperatures and gives rise to enhanced MR<sub>xx</sub>.<sup>4</sup> However, the presence of defects and atomic disorders will cause significant impurity scattering at low temperatures and suppress the MR effect giving rise to low-temperature maximum in MRxxl, followed by a drastic drop. 42 Therefore, the absence of such low-temperature maximum in our l  $MR_{xx}(\mu_0 H = 2 \text{ T})$  data indicates that the degree of atomic

disorder and defects is not significant in our MgO/CoFeCrGa films compared to the other SGS films. 41,42

Since the MR<sub>xx</sub> in SGS materials is dominated by the spindependent scattering mechanism, we have analyzed the MR<sub>xx</sub>(H) data for our MgO/CoFeCrGa (95 nm) film using the Khosla and Fischer model, <sup>4 §</sup>  $MR_{xx}(H) = -a^2 \ln(1+b^2H^2) + \left(\frac{c^2H^2}{1+d^2H^2}\right)$ , where the first term originates from the spin-dependent scattering of carriers by localized magnetic moments and gives rise to negative  $MR_{xxy}$  whereas the second term represents the contribution from two-carrier conduction channels and gives rise to positive MR<sub>xx</sub>. Here,  $a = [A_1 J_{\rm ex} D(E_{\rm F}) \{ S(S+1) + \langle M^2 \rangle \}]^{1/2}$  and  $b = \left[1 + 4\pi^2 S^2 \left(\frac{2J_{\rm ex} D(E_{\rm F})}{g}\right)\right]^{1/2} \left(\frac{g\mu_B}{\beta k_B T}\right)$ , where  $A_1$  is a constant representing the contribution of spin-dependent scattering toward MR<sub>xx</sub>,  $J_{ex}$  is the s-d exchange integral,  $D(E_F)$  is the density of states at the Fermi level, S represents the spin of the localized magnetic moment,  $\langle M^2 \rangle$  is the average of the squared magnetization, g is the Landé g-factor,  $k_{\rm B}$  is the Boltzmann constant, and  $\beta$  is the numerical constant. Also, the coefficients  $c^2$  and  $d^2$  are given by  $c^2 = \frac{\sigma_1 \sigma_2 (\mu_1 + \mu_2)^2}{(\sigma_1 + \sigma_2)^2}$  and  $d^2 = \frac{(\sigma_i \mu_2 - \sigma_2 \mu_1)^2}{(\sigma_1 + \sigma_2)^2}$ , where  $\sigma_i$  and  $\mu_i$  represent the conductivity and mobility of the ith carrier channel. 44 According to the twocarrier conduction channel model or the two-band model, carrier transport occurs through two distinct bands (conduction band and impurity band) with different conductivities and mobilities for majority and minority spin carriers. 43 Application of magnetic field gives rise to enhanced scattering of spin-polarized carriers due to changes in the local Zeeman potential because of which positive magnetoresistance results in. 44 Note that we have tried to fit the  $MR_{xx}(H)$  data for our MgO/CoFeCrGa (95 nm) film considering only the contribution of negative magnetoresistance, i.e., with the expression,  $MR_{xx}(H) = -a^2 \ln(1 + b^2H^2)$ , but it did not fit well in the high-field region (see Figure S7). Considering the fact that some of the SGS materials exhibit positive MRxx at low temperatures, <sup>26,45</sup> and the two-carrier conduction channel model is often used to analyze the  $MR_{xx}(H)$  data for those SGS materials,<sup>45</sup> we believe that there is a minor contribution of positive MRxx, which is dominated by the negative MRxx contribution in our MgO/CoFeCrGa (95 nm) film. We found that the MR<sub>xx</sub>(H) data for our MgO/CoFeCrGa (95 nm) film is well fitted to the combined expression  $MR_{xx}(H) = -a^2 ln(1+b^2H^2) + \left(\frac{c^2H^2}{1+d^2H^2}\right)$  for the entire measured temperature range. The temperature dependence of the fitting parameters is shown in Figure 4c,d). Evidently, all the fitting parameters show noticeable changes around the temperature region where both  $\rho_{xx}(T)$  and  $MR_{xx}(T)$  exhibit change in slope. Furthermore, lal is nearly 3 orders of magnitude higher than |c| at all temperatures, indicating that the negative MR<sub>xx</sub> originated from the spin-dependent scattering primarily governs the electronic transport. The insignificant contribution of the impurity-driven two carrier channel conduction toward the observed MRxx further implies that the atomic disorder and defects are negligible in our

We have also performed radio frequency (RF) transverse susceptibility (TS) measurements on our MgO/CoFeCrGa

MgO/CoFeCrGa (95 nm) film.

film in the temperature range 20 K  $\leq$   $T \leq$  300 K to determine the temperature evolution of effective magnetic anisotropy. This technique can accurately determine the dynamical magnetic response of a magnetic material in the presence of a DC magnetic field  $(H_{DC})$  and a transverse RF magnetic field  $(H_{RF})$  with small and fixed amplitude.<sup>30</sup> When  $H_{DC}$  is scanned from positive to negative saturations, the TS of a magnetic material with uniaxial anisotropy demonstrates well-defined peaks at the anisotropy fields,  $\hat{H}_{DC} = \pm H_K^{30}$  However, for a magnetic material comprising randomly dispersed magnetic easy axes, the TS shows broad maxima at the effective anisotropy fields,  $H_{\rm DC}=\pm H_{\rm K}^{\rm \,eff}.$  Here, we show the TS spectra as percentage change of the measured transverse susceptibility as  $\frac{\Delta \chi_T}{\chi_T}(H_{\rm DC}) = \frac{\chi_T(H_{\rm DC}) - \chi_T(H_{\rm DC}^{\rm max})}{\chi_T(H_{\rm DC}^{\rm max})} \times 100\%$ , where  $\chi_T(H_{\rm DC}^{\rm max})$  is the value of  $\chi_T$  at the maximum value of the applied DC magnetic field,  $H_{\rm DC}^{\rm max}$  which is chosen in such a way that  $H_{\rm DC}^{\rm max} \gg H_{\rm DC}^{\rm sat}$ , where  $H_{\rm DC}^{\rm sat}$  is the saturation magnetic field. Figure 3e shows the bipolar field scan  $(+H_{\rm DC}^{\rm max} \to -H_{\rm DC}^{\rm max} \to +H_{\rm DC}^{\rm max})$  $H_{\mathrm{DC}}^{\mathrm{max}}$ ) of  $\frac{\Delta \chi_{T}}{\chi_{T}}(H_{\mathrm{DC}})$  for the MgO/CoFeCrGa film measured at T = 20 K for both IP ( $H_{DC}$  || film surface) and OOP ( $H_{DC} \perp$ film surface) configurations. For both the configurations, the TS shows maxima centering at  $H_{DC} = \pm H_K^{\text{eff}}$ . Here, we define  $H_{\rm K}^{\rm eff}=H_{\rm K}^{\rm IP}$  as the IP effective anisotropy field (for IP configuration) and  $H_{\rm K}^{\rm eff}=H_{\rm K}^{\rm OOP}$  as the OOP effective anisotropy field (for OOP configuration). We found that I  $H_{\rm K}^{\rm OOP}|>|H_{\rm K}^{\rm IP}|$  at all the temperatures indicating IP easy axis of this film in the temperature range 20 K  $\leq$  T  $\leq$  300 K. Furthermore, it is evident that the peaks at  $+H_{K}^{IP}(+H_{K}^{OOP})$ and  $-H_K^{\text{IP}}(-H_K^{\text{OOP}})$  are asymmetric with unequal peak heights, which is indicative of significant anisotropy dispersion in our MgO/CoFeCrGa film for the both IP and OOP configurations. The temperature variations of  $H_{\rm K}^{\ \rm IP}$  and  $H_{\rm K}^{\ \rm OOP}$ for our MgO/CoFeCrGa (95 nm) film are shown in Figure 3f. Clearly, both  $H_{\rm K}^{\rm IIP}$  and  $H_{\rm K}^{\rm OOP}$  increase with decreasing temperature and  $H_{\rm K}^{\rm OOP}$  >  $H_{\rm K}^{\rm IIP}$  throughout the measured temperature range. Interestingly, with decreasing temperature,  $H_{\rm K}^{\rm OOP}$  increases more rapidly than  $H_{\rm K}^{\rm IP}$ , which gives rise to large difference between  $H_{\rm K}^{\rm IP}$  and  $H_{\rm K}^{\rm OOP}$  at low temperatures. Additionally, both  $H_{\rm K}^{\rm IP}$  and  $H_{\rm K}^{\rm OOP}$  increases more rapidly below  $\approx$ 200 K compared to the temperature range of 20 K  $\leq$  T

3.3. Thermal Spin Transport Properties: ANE and **LSSE.** Next, we focus on the thermo-spin transport properties of our MgO/CoFeCrGa (95 nm) film. We have performed anomalous Nernst effect (ANE) and longitudinal spin Seebeck effect (LSSE) measurements on MgO/CoFeCrGa (95 nm) and MgO/CoFeCrGa (95 nm)/Pt (5 nm) films, respectively. Figure 5a,b demonstrates the schematic illustrations of our ANE and LSSE measurements. Both the ANE and LSSE measurements on MgO/CoFeCrGa (95 nm) and MgO/ CoFeCrGa (95 nm)/Pt films, respectively, were performed by sandwiching the film between two copper blocks and applying a temperature gradient (along the +z-direction) that creates a temperature difference,  $\Delta T$ , between those copper blocks in the presence of an external DC magnetic field applied along the x-direction. The thermally generated Nernst and LSSE voltages generated along the y-direction were recorded using a Keithley 2182a nanovoltmeter while scanning the DC magnetic field. According to the theory of thermally generated magnon-driven interfacial spin pumping mechanism, simultaneous application of a vertical (z-axis) temperature gradient

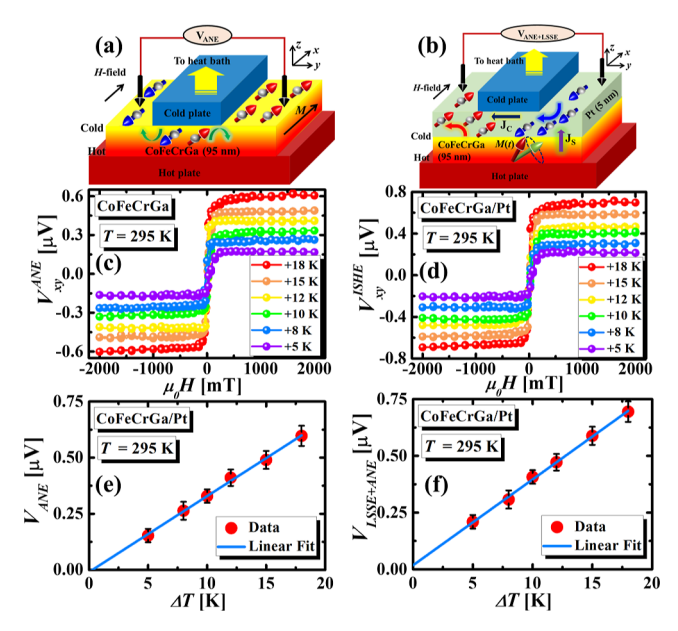


Figure 5. (a,b) Schematic illustrations of our ANE and LSSE measurements, respectively. (c,d) Magnetic field dependence of the ANE voltage,  $V_{\rm ANE}(H)$ , and ISHE-induced in-plane voltage,  $V_{\rm ISHE}(H)$  measured on the MgO/CoFeCrGa (95 nm) and MgO/CoFeCrGa (95 nm)/Pt films, respectively, for different values of the temperature difference between the hot  $(T_{\rm hot})$  and cold  $(T_{\rm cold})$  copper blocks,  $\Delta T = (T_{\rm hot} - T_{\rm cold})$ , in the range +5 K $\leq$   $\Delta T \leq$  +18 K at a fixed average sample temperature  $T = \frac{T_{\rm hot} + T_{\rm cold}}{2} = 295$  K. (e,f)  $\Delta T$  dependence of the back ground-corrected ANE voltage,  $V_{\rm ANE}(\Delta T) = \left[\frac{V_{\rm ANE}(+\mu_0 H_{\rm max}, \Delta T) - V_{\rm ANE}(-\mu_0 H_{\rm max}, \Delta T)}{2}\right]$ , and the background-corrected (ANE + LSSE) voltage,  $V_{\rm ANE+LSSE}(\Delta T) = \left[\frac{V_{\rm ISHE}(+\mu_0 H_{\rm max}, \Delta T) - V_{\rm ISHE}(-\mu_0 H_{\rm max}, \Delta T)}{2}\right]$ .

 $(\nabla T)$  and an external transverse dc magnetic field  $(\mu_0 H)$ (x-axis) across the MgO/CoFeCrGa (95 nm)/Pt film gives rise to transverse spin current pumping from the CoFeCrGa layer into the Pt layer with the interfacial spin current density:  $\overrightarrow{J_{
m S}} = rac{G^{\uparrow\downarrow}}{2\pi} rac{\gamma h}{M_{
m S} V_{
m A}} k_{
m B} \overrightarrow{\nabla T}$  at the CoFeCrGa/Pt interface, where  $G^{\uparrow\downarrow}$ ,  $\hbar$ ,  $\gamma$ ,  $M_{\rm S}$ , and  $V_{\rm a}$  are the interfacial spin-mixing conductance, the reduced Planck's constant  $\left(\hbar = \frac{h}{2\pi}\right)$ , the gyromagnetic ratio, the saturation magnetization of CoFeCrGa, and the magnon coherence volume, respectively. <sup>22,46,47</sup> The magnetic coherence volume is expressed as  $V_{\rm a}=\frac{2}{3\zeta(5/2)}\Big(\frac{4\pi D}{k_{\rm B}T}\Big)^{3/2}$  , where  $\zeta$  is the Riemann Zeta function and D is the spin-wave stiffness constant. This transverse spin current,  $J_s$ , is then converted into charge current  $\overrightarrow{J_{\rm C}} = \left(\frac{2\ell}{\hbar}\right)\theta_{\rm SH}^{\rm Pt}(\overrightarrow{J_{\rm S}}\times\overrightarrow{\sigma_{\rm S}})$  along the y-axis via the inverse spin Hall effect (ISHE), where e,  $\theta_{\rm SH}^{\rm Pt}$ , and  $\sigma_{\rm S}$  are the electron charge, the spin Hall angle of Pt, and the spin polarization vector, respectively. The corresponding voltage along the y-axis can be expressed as 22,48

$$V_{\rm LSSE} = R_{\rm y} L_{\rm y} \lambda_{\rm Pt} \left(\frac{2e}{\hbar}\right) \theta_{\rm SH}^{\rm Pt} J_{\rm S} \tan h \left(\frac{t_{\rm Pt}}{2\lambda_{\rm Pt}}\right) \tag{1}$$

where  $R_y$ ,  $L_y$ ,  $\lambda_{Pt}$  and  $t_{Pt}$  are the electrical resistance between the voltage leads, the distance between the voltage leads, the

spin diffusion length of Pt, and the thickness of the Pt layer (=5 nm), respectively. Since CoFeCrGa is a spin gapless semiconductor with soft ferromagnetic behavior, 28,35 concomitant application of the temperature gradient (z-axis) and dc magnetic field (x-axis) also generates a spin-polarized current in the CoFeCrGa layer along the y-axis due to ANE, 49 which gives rise to an additional contribution ( $V_{\mathrm{CoFeCRGa}}^{\mathrm{ANE}}$ ) to the total voltage signal measured across the Pt layer in the MgO/ CoFeCrGa (95 nm)/Pt heterostructure.

In the presence of a transverse temperature gradient ( $\nabla T$ ), the electric field generated by ANE in a magnetic conductor/ semiconductor with magnetization M can be expressed as

$$\overrightarrow{E_{\text{ANE}}} \propto S_{\text{ANE}}(\mu_0 \vec{M} \times \overrightarrow{\nabla T}) \tag{2}$$

where  $S_{ANE}$  is the anomalous Nernst coefficient. Furthermore, an additional voltage contribution  $(V_{\text{Prox}}^{\text{ANE}})$  can appear due to the magnetic proximity effect (MPE)-induced ANE in the nonmagnetic Pt layer.4

Note that only a few layers of Pt close to the MgO/ CoFeCrGa (95 nm)/Pt interface gets magnetized (proximitized) due to the MPE, whereas the remaining layers remain unmagnetized. Hence, both  $V_{\text{CoFeCRGa}}^{\text{ANE}}$  and  $V_{\text{Prox}}^{\text{ANE}}$  are suppressed due to the inclusion of the 5 nm-thick Pt layer on top of the CoFeCrGa layer.<sup>21</sup> Therefore, the resultant voltage measured across the Pt layer of our MgO/CoFeCrGa (95 nm)/Pt heterostructure can be expressed as  $^{50}$   $V_{\rm ANE+LSSE} = V_{\rm LSSE} + V_{\rm CoFeCRGa,Sup}^{\rm ANE} + V_{\rm Prox,Sup}^{\rm ANE}$ , where  $V_{\rm CoFeCRGa,Sup}^{\rm ANE}$  and  $V_{\rm Prox,Sup}^{\rm ANE}$  account for the suppressed ANE voltages due to the CoFeCrGa layer and the MPE-induced ANE voltage in the Pt layer, respectively. Previous studies show that the contribution from the MPE-induced ANE in the Pt layer is negligibly small for bilayers consisting of magnetic semi-conductors and Pt.<sup>21,49</sup> Also, in our previous report,<sup>50</sup> we have shown that the MPE-induced LSSE contribution of the proximitized Pt layer is negligible as only a few layers of Pt close to the CoFeCrGa (95 nm)/Pt interface are magnetized due to the MPE.<sup>21</sup> Therefore, the resultant voltage measured across the Pt layer of our MgO/CoFeCrGa (95 nm)/Pt heterostructure can be expressed as  $V_{\mathrm{ANE+LSSE}} = V_{\mathrm{LSSE}}$  +  $V_{\text{CoFeCRGa,Sup}}^{\text{ANE}}$ . Considering a parallel circuit configuration of CoFeCrGa and Pt layers, the suppressed ANE voltage (due to the CoFeCrGa layer) across the Pt layer of the MgO/ CoFeCrGa(95 nm)/Pt heterostructure can be expressed as 21,49

$$V_{\text{CoFeCrGa},\text{Sup}}^{\text{ANE}} = \left(\frac{F}{1+F}\right) V_{\text{CoFeCrGa}}^{\text{ANE}} \tag{3}$$

where  $F = \frac{\rho_{\rm Pt}}{\rho_{\rm CoFeCrGa}} \cdot \frac{t_{\rm CoFeCrGa}}{t_{\rm Pt}}$ ,  $\rho_{\rm CoFeCrGa}$  ( $\rho_{\rm Pt}$ ) is the electrical resistivity of the CoFeCrGa (Pt) layer, and  $t_{\text{CoFeCrGa}}\left(t_{\text{Pt}}\right)$  is the thickness of the CoFeCrGa (Pt) layer, respectively. Therefore, the intrinsic LSSE voltage contribution can be disentangled from the ANE contribution using the expression<sup>21,50</sup>

$$V_{\rm LSSE} = V_{\rm ANE+LSSE} - \left(\frac{F}{1+F}\right) V_{\rm CoFeCrGa}^{\rm ANE} \tag{4}$$

Figure 5c,d shows the magnetic field dependence of the ANE voltage,  $V_{\text{ANE}}(H)$ , and ISHE-induced in-plane voltage, V<sub>ISHE</sub>(H), measured on the MgO/CoFeCrGa (95 nm) and MgO/CoFeCrGa (95 nm)/Pt films, respectively, for different values of the temperature difference between the hot  $(T_{hot})$ and cold  $(T_{\text{cold}})$  copper blocks,  $\Delta T = (T_{\text{hot}} - T_{\text{cold}})$ , in the

range +5 K $\leq$   $\Delta T$   $\leq$  +18 K at a fixed average sample temperature  $T = \frac{T_{\text{hot}} + T_{\text{cold}}}{2} = 295 \text{ K. Clearly, both } V_{\text{ANE}}(H)$  and  $V_{\rm ISHE}(H)$  signals increase upon increasing  $\Delta T$ . Figure 5e,f exhibits the  $\Delta T$  dependence of the background-corrected ANE voltage,  $V_{\text{ANE}}(\Delta T) = \left[\frac{V_{\text{ANE}}(+\mu_0 H_{\text{max}}, \Delta T) - V_{\text{ANE}}(-\mu_0 H_{\text{max}}, \Delta T)}{V_{\text{ANE}}(-\mu_0 H_{\text{max}}, \Delta T)}\right]$ the background-corrected (ANE + LSSE) voltage,  $V_{\mathrm{ANE+LSSE}}(\Delta T) = \begin{bmatrix} v_{\mathrm{ISHE}}(+\mu_0 H_{\mathrm{max}}, \Delta T) - v_{\mathrm{ISHE}}(-\mu_0 H_{\mathrm{max}}, \Delta T) \\ 2 \end{bmatrix},$  $\mu_0 H_{\rm max}$   $(\mu_0 H_{\rm max} \gg \mu_0 H_{\rm sat})$  is the maximum value of the applied magnetic field strength and  $\mu_0 H_{\text{sat}}$  = saturation magnetic field. Evidently, both  $V_{
m ANE}$  and  $V_{
m ANE+LSSE}$  scale linearly with  $\Delta T$  and  $|V_{\text{ANE+LSSE}}| > |V_{\text{ANE}}|$ , which confirm that the observed field dependences originate from ANE and (ANE + LSSE), respectively.<sup>21,50</sup>

In Figure 6a,b, we show  $V_{\text{ANE}}(H)$  and  $V_{\text{ISHE}}(H)$  hysteresis loops measured at selected average sample temperatures in the

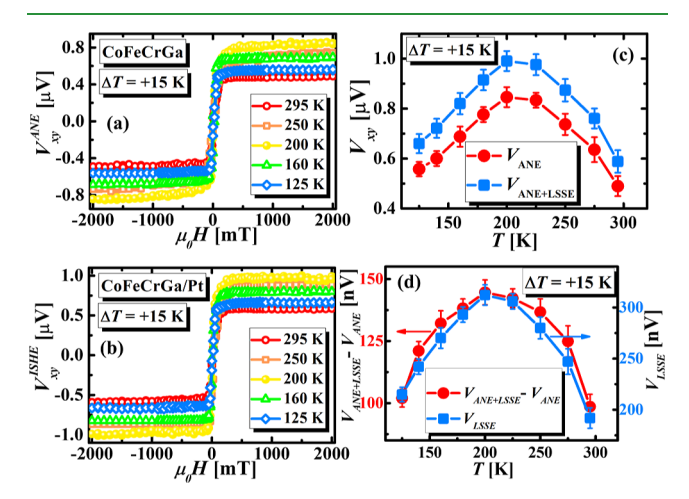


Figure 6. (a,b)  $V_{ANE}(H)$  and  $V_{ISHE}$  hysteresis loops measured at selected average sample temperatures in the temperature range 125  $K \le \Delta T \le 295$  K for a fixed value of  $\Delta T = +15$  K on MgO/CoFeCrGa (95 nm) and MgO/CoFeCrGa (95 nm)/Pt films, respectively. (c) Tdependence of the background-corrected ANE voltage, 
$$\begin{split} V_{\text{ANE}}(T) &= \left[\frac{v_{\text{ANE}}(+\mu_0 H_{\text{max}}, T) - v_{\text{ANE}}(-\mu_0 H_{\text{max}}, T)}{2}\right] \text{, and the background-} \\ \text{corrected} & \left(\begin{array}{ccc} A \text{ N E} &+ & L \text{ S S E} \end{array}\right) & \text{voltage,} \\ V_{\text{ANE+LSSE}}(T) &= \left[\frac{v_{\text{ISHE}}(+\mu_0 H_{\text{max}}, T) - v_{\text{ISHE}}(-\mu_0 H_{\text{max}}, T)}{2}\right] \text{, measured on} \end{split}$$
MgO/CoFeCrGa (95 nm) and MgO/CoFeCrGa (95 nm)/Pt films. (d) Right y-scale: the temperature dependence of the intrinsic LSSE voltage,  $V_{LSSE}(T)$ , and the left y-scale: the temperature dependence of  $[V_{\text{ANE+LSSE}}(T) - V_{\text{ANE}}(T)].$ 

temperature range 125 K  $\leq \Delta T \leq$  295 K for a fixed value of  $\Delta T$ = +15 K on MgO/CoFeCrGa (95 nm) and MgO/CoFeCrGa (95 nm)/Pt films. Figure 6c exhibits the T-dependence of the background-corrected ANE voltage,  $V_{\mathrm{ANE}}(T) = \left[\frac{V_{\mathrm{ANE}}(+\mu_0 H_{\mathrm{max}}, T) - V_{\mathrm{ANE}}(-\mu_0 H_{\mathrm{max}}, T)}{2}\right], \quad \text{and the back-}$ on MgO/CoFeCrGa (95 nm) and MgO/CoFeCrGa (95 nm)/Pt films, respectively. It is evident that both  $|V_{ANE}(T)|$ and  $|V_{\text{ANE+LSSE}}(T)|V_{\text{ANE}}$  increase with decreasing temperature up to T = 200 K below which both of them decrease gradually with further reducing the temperature, resulting in a maximum

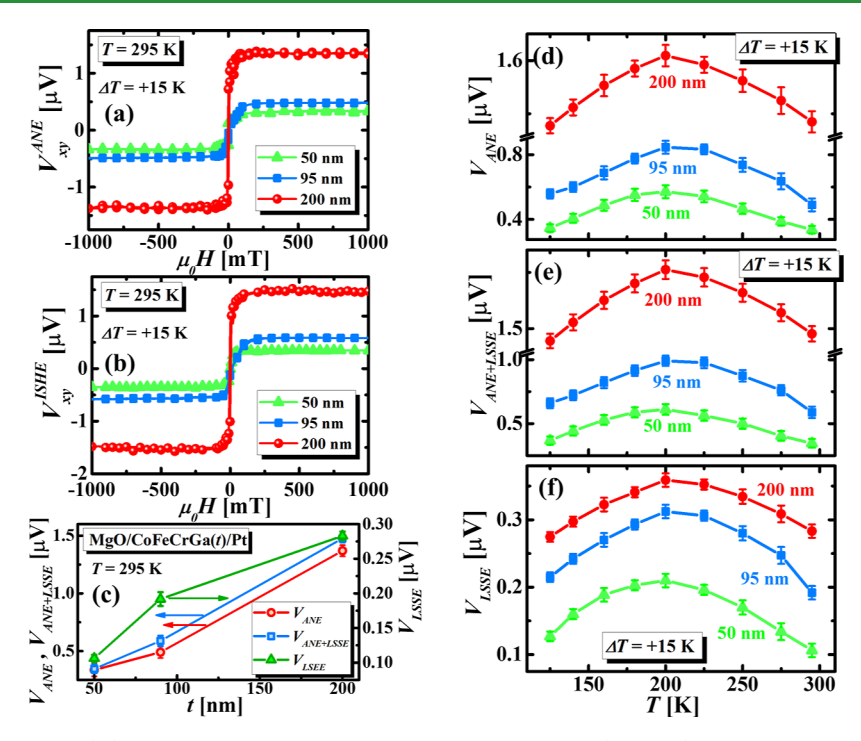


Figure 7. (a,b)  $V_{\text{ANE}}(H)$  and  $V_{\text{ISHE}}(H)$  hysteresis loops measured on the MgO/CoFeCrGa( $t_{\text{CoFeCrGa}}$ ) and MgO/CoFeCrGa( $t_{\text{CoFeCrGa}}$ )/Pt films for  $t_{\text{CoFeCrGa}}$ (CoFeCrGa film thickness) = 50, 95, and 200 nm at 295 K for  $\Delta T$  = +15 K. (c)  $V_{\text{ANE}}(\mu_0 H$  = 1 T),  $V_{\text{ANE+LSSE}}(\mu_0 H$  = 1 T), and  $V_{\text{LSSE}}(\mu_0 H$  = 1 T) at 295 K plotted as a function of  $t_{\text{CoFeCrGa}}$ . (d-f) Comparison of  $V_{\text{ANE}}(T)$ ,  $V_{\text{ANE+LSSE}}(T)$ , and  $V_{\text{LSSE}}(T)$ , respectively, for different  $t_{\text{CoFeCrGa}}$ .

around 200 K. Furthermore,  $|V_{\rm ANE+LSSE}(T)| > |V_{\rm ANE}(T)|$  throughout the measured temperature range, which confirms that both ANE and LSSE contribute toward the voltage measured on the MgO/CoFeCrGa (95 nm)/Pt heterostructure.

In order to determine the temperature dependence of intrinsic LSSE voltage, we have disentangled the LSSE contribution from the ANE contribution using eq 4. The right y-scale of Figure 6d shows the temperature dependence of the intrinsic LSSE voltage,  $V_{\rm LSSE}(T)$ , obtained by using eq 4 by incorporating the correction factor,  $\left(\frac{F}{1+F}\right)$ , whereas the left y-scale shows the temperature dependence of the voltage difference  $[V_{\text{ANE+LSSE}}(T) - V_{\text{ANE}}(T)]$  without incorporating the aforementioned correction factor, for comparison. A clear distinction can be observed between  $V_{LSSE}(T)$  and  $[V_{\text{ANE+LSSE}}(T) - V_{\text{ANE}}(T)]$  in terms of the absolute value as well the nature of the T-dependence, highlighting the importance of the correction factor for accurately determining the intrinsic LSSE contribution. Evidently,  $|V_{LSSE}(T)|$  increases with decreasing temperature and shows a broad maximum around 200 K below which it decreases gradually with further lowering the temperature, as shown in Figure 6d. To ensure that the observed behavior of  $V_{ANE}(T)$  and  $V_{LSSE}(T)$  is intrinsic to the MgO/CoFeCrGa (95 nm) and CoFeCrGa (95 nm)/Pt films, respectively, we repeated the same experiments for two more CoFeCrGa films with different thicknesses, namely,  $t_{\text{CoFeCrGa}} = 50$  and 200 nm. The temperaturedependent magnetometry and DC electrical transport properties of the  $t_{\text{CoFeCrGa}} = 50$  and 200 nm films are displayed in the Supporting Information (Figures S1 and S3, respectively). Furthermore, similar to the  $t_{\text{CoFeCrGa}} = 95 \text{ nm}$  film, both  $V_{\text{ANE}}$ and  $V_{\rm ANE+LSSE}$  for  $t_{\rm CoFeCrGa}$  = 50 and 200 nm films scale linearly with  $\Delta T$  and  $|V_{\text{ANE+LSSE}}| > |V_{\text{ANE}}|$ , as shown in Figure S5. In Figure S6, we demonstrate  $V_{ANE}(H)$  and  $V_{ISHE}(H)$  hysteresis

loops at selected average sample temperatures in the range 125  $K \leq \Delta T \leq 295$  K for a fixed value of  $\Delta T = +15$  K for  $t_{\text{CoFeCrGa}}$ = 50 and 200 nm films. In Figure 7a,b, we compare  $V_{\rm ANE}(H)$ and  $V_{\rm ISHE}(H)$  hysteresis loops measured on the MgO/  $CoFeCrGa(t_{CoFeCrGa})$  and  $MgO/CoFeCrGa(t_{CoFeCrGa})/Pt$ films for  $t_{\text{CoFeCrGa}}$  (CoFeCrGa film thickness) = 50, 95, and 200 nm at T = 295 K for  $\Delta T = +15$  K. As shown in Figure 7c,  $V_{\text{ANE}}(\mu_0 H = 1 \text{ T})$ ,  $V_{\text{ANE+LSSE}}$  ( $\mu_0 H = 1 \text{ T}$ ), and  $V_{\text{LSSE}}(\mu_0 H = 1 \text{ T})$ T) at 295 K increase with increasing  $t_{\text{CoFeCrGa}}$ . In Figure 7d–f, we compare  $V_{\text{ANE}}(T)$ ,  $V_{\text{ANE+LSSE}}(T)$ , and  $V_{\text{LSSE}}(T)$ , respectively, for different  $t_{\text{CoFeCrGa}}$ . Clearly, the values of all the three quantities,  $V_{\rm ANE}$ ,  $V_{\rm ANE+LSSE}$ , and  $V_{\rm LSSE}$ , are higher for thicker CoFeCrGa films at all temperatures. Furthermore,  $|V_{ANE}(T)|$ , |  $V_{\text{ANE+LSSE}}(T)$ , and  $|V_{\text{ANE}}(T)|$  exhibit the same behavior for all the three different CoFeCrGa film thicknesses, i.e., all these quantities increase with decreasing temperature from 295 K and show a broad maximum around 200 K, which is followed by a gradual decrease with further lowering the temperature. These observations confirm that the observed behavior of  $V_{\text{ANE}}(T)$  and  $V_{\text{LSSE}}(T)$  is intrinsic to the MgO/CoFeCrGa and MgO/CoFeCrGa/Pt films, respectively.

**3.4. Mechanism of LSSE** and **ANE** at Low Temperatures. Since the density of the thermally generated magnons-driven spin current is proportional to the effective temperature gradient across the CoFeCrGa film through the expression,  $|\overrightarrow{J_S}| = \frac{G^{11}}{2\pi} \frac{\gamma h}{M_S V_a} k_B | \overrightarrow{\nabla T}|$ , it is imperative to accurately determine the effective temperature differences between the top and bottom surfaces of the CoFeCrGa film ( $\Delta T_{\rm eff}$ ). The total temperature difference ( $\Delta T$ ) across the MgO/CoFeCrGa (95 nm)/Pt heterostructure can be expressed as a linear combination of temperature drops in the Pt layer, at the Pt/CoFeCrGa interface, in the CoFeCrGa layer, at the CoFeCrGa/MgO interface, across the GSGG substrate, as well as in the N-grease layers (thickness  $\approx 1~\mu m$ ) on both sides

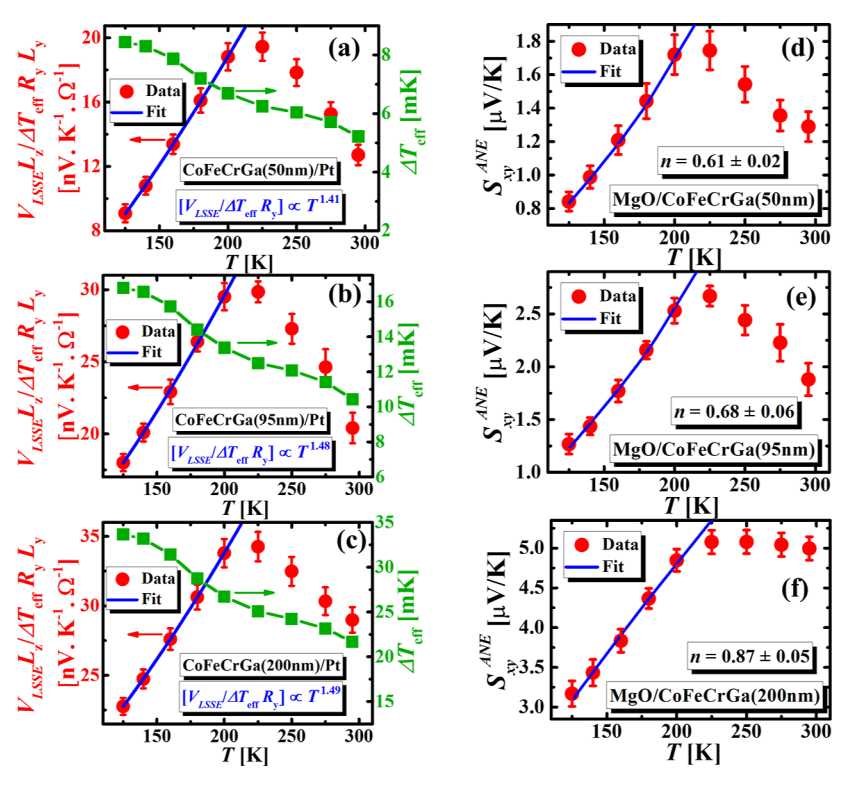


Figure 8. (a-c) Right y-scale: temperature dependence of  $\Delta T_{\rm eff}$  for different  $t_{\rm CoFeCrGa}$ , left y-scale: temperature dependence of the modified LSSE coefficient,  $S_{\rm LSSE}^{\rm eff}(T)$ , for MgO/CoFeCrGa( $t_{\rm CoFeCrGa}$ )/Pt (5 nm) films for  $t_{\rm CoFeCrGa}$  = 50, 95, and 200 nm, respectively, fitted with the expression  $S_{\rm LSSE}^{\rm eff} \propto \left(\theta_{\rm SH}^{\rm Pt} \frac{G^{11}}{2\pi} \frac{k_{\rm B}}{D^{3/2}}\right) T^{\rm n}$ . (d-f) Temperature dependence of the ANE coefficient,  $S_{\rm xy}^{\rm ANE}(T)$ , for the MgO/CoFeCrGa( $t_{\rm CoFeCrGa}$ ) films for  $t_{\rm CoFeCrGa}$  = 50, 95, and 200 nm, respectively, fitted with eq 6.

of the MgO/CoFeCrGa/Pt heterostructure, and can be written as,  $^{51}$   $\Delta T = \Delta T_{\rm Pt} + \Delta T_{\rm Pt/CoFeCrGa} + \Delta T_{\rm CoFeCrGa} + \Delta T_{\rm CoFeCrGa} + \Delta T_{\rm CoFeCrGa/MgO} + \Delta T_{\rm MgO} + 2.\Delta T_{\rm N-Grease}.$  Since the thermal resistance of Pt is very small compared to the other contributions and the bulk contributions toward the measured ISHE voltage dominate over the interfacial contributions when the thickness of the magnetic film (CoFeCrGa) is high enough,  $^{51}$  the total temperature difference can be approximately written as  $\Delta T = \Delta T_{\rm CoFeCrGa} + \Delta T_{\rm MgO} + 2.\Delta T_{\rm N-Grease}.$  Considering the 4-slab model, the total thermal resistance between hot and cold plates can be written as,

$$R_{\mathrm{Th}} = \frac{1}{A} \left( \frac{2t_{\mathrm{N-Grease}}}{\kappa_{\mathrm{N-Grease}}} + \frac{t_{\mathrm{CoFeCrGa}}}{\kappa_{\mathrm{CoFeCrGa}}} + \frac{t_{\mathrm{MgO}}}{\kappa_{\mathrm{MgO}}} \right)$$
, where  $t_{\mathrm{N-Grease}}$ ,  $t_{\mathrm{MgO}}$ , and

 $t_{\text{CoFeCrGa}}$  are the thicknesses of the grease layers, MgO substrate, and the CoFeCrGa layer, respectively;  $\kappa_{\text{N-Grease}}$ ,  $\kappa_{\text{MgO}}$ , and  $\kappa_{\text{CoFeCrGa}}$  are the thermal conductivities of the grease layers, MgO substrate, and CoFeCrGa layer, respectively, and A is the cross-sectional area. Since the rate of heat flow across the entire heterostructure reaches a constant value in the steady state, the effective temperature difference across the CoFeCrGa film can be written as  $^{22}$ 

$$\Delta T_{\text{eff}} = \Delta T_{\text{CoFeCrGa}} = \frac{\Delta T}{\left[1 + \frac{\kappa_{\text{CoFeCrGa}}}{t_{\text{CoFeCrGa}}} \left(\frac{2t_{\text{N-Grease}}}{\kappa_{\text{N-Grease}}} + \frac{t_{\text{MgO}}}{\kappa_{\text{MgO}}}\right)\right]}$$
(5)

We have measured the temperature dependence of thermal conductivity of bulk CoFeCrGa using the thermal transport option of the PPMS, as shown in the Supporting Information (Figure S4). Using the reported values of the thermal conductivities of the Apiezon N-grease, <sup>52</sup> and the MgO

crystal,  $^{53}$  we have determined the temperature dependence of  $\Delta T_{\rm eff}$  for different  $t_{\rm CoFeCrGa}$  using eq 5, as shown in Figure 8a–c. Here, we have ignored the interfacial thermal resistances between the N-grease and the hot/cold plates as well as between the sample and N-grease layers.  $^{8}$ 

Using the T-dependence of  $\Delta T_{\rm eff}$ , we have estimated the T-dependence of the modified LSSE coefficient,

$$S_{\text{LSSE}}^{\text{eff}}(T) = \frac{V_{\text{LSSE}}(T)}{\Delta T_{\text{eff}}(T)R_{\text{y}}(T)} \times \left(\frac{L_{z}}{L_{\text{y}}}\right), \text{ for } \text{MgO/CoFeCrGa}$$

 $(t_{\text{CoFeCrGa}})/\text{Pt}$  (5 nm) films for  $t_{\text{CoFeCrGa}} = 50$ , 95, and 200 nm, where  $L_v$  (=3 mm) is the distance between the voltage leads and  $L_z = t_{\text{CoFeCrGa}}$  (see Figure 8a-c). Note that we have measured the T-dependence of resistance,  $R_v(T)$  between the voltage leads placed on the Pt layer of the MgO/CoFeCrGa- $(t_{\text{CoFeCrGa}})/\text{Pt}$  heterostructures using four-point probe configuration. Note that the value of  $S_{LSSE}^{eff}(T)$  for our MgO/ CoFeCrGa( $t_{\text{CoFeCrGa}}$ )/Pt heterostructures are  $\approx$ 12.8, 20.5, and 29.8 nV K<sup>-1</sup>  $\Omega^{-1}$  at T=295 K for  $t_{\text{CoFeCrGa}}=50$ , 95, and 200 nm, respectively, which are higher than those of the halfmetallic FM thin films of  $La_{0.7}Sr_{0.3}MnO_3$  ( $\approx 9$  nV K<sup>-1</sup>  $\Omega^{-1}$  at room temperature).<sup>23</sup> As shown in Figure 8a-c,  $S_{LSSE}^{eff}(T)$  for the MgO/CoFeCrGa( $t_{CoFeCrGa}$ )/Pt (5 nm) heterostructures for all the three CoFeCrGa film thicknesses increases as T decreases from room temperature and shows a peak around 225 K below which it decreases rapidly with a further decrease in temperature.

Since the saturation magnetization,  $M_{\rm S} \approx T^{-1}$  in the measured temperature range (as shown in Figure 3a) and  $V_{\rm a} \propto T^{-3/2}$  according to the theory of magnon-driven LSSE,  $|\overrightarrow{J_{\rm S}}| \propto \frac{G^{14}}{2\pi} \frac{k_{\rm B}}{D^{3/2}} T^{5/2} |\overrightarrow{\nabla T}|^{22}$  Considering  $\tanh\left(\frac{t_{\rm Pt}}{2\lambda_{\rm Pt}}\right) \approx 1$  for our

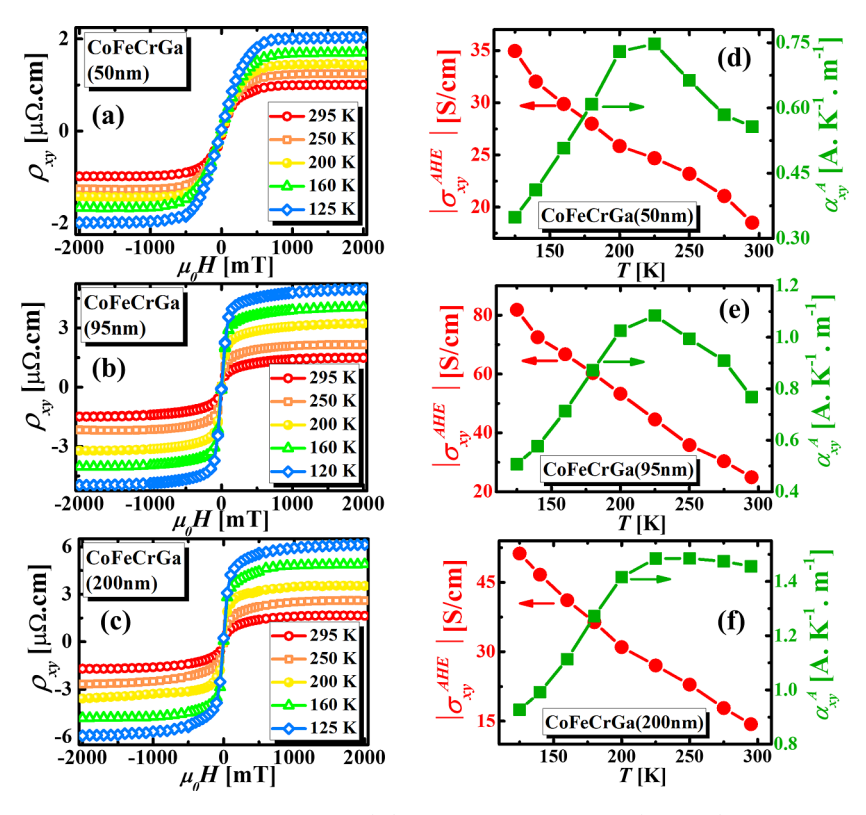


Figure 9. (a–c) Magnetic field dependence of Hall resistivity  $\rho_{xy}(H)$  of our MgO/CoFeCrGa( $t_{\text{CoFeCrGa}}$ ) films for  $t_{\text{CoFeCrGa}}$  = 50, 95, and 200 nm, respectively, recorded at few selected temperatures in the range 125 K  $\leq T \leq$  295 K. (d–f) Left y-scale: the temperature dependence of the anomalous Hall conductivity,  $|\sigma_{xy}|^{AHE}$ , of our MgO/CoFeCrGa( $t_{\text{CoFeCrGa}}$ ) films for  $t_{\text{CoFeCrGa}}$  = 50, 95, and 200 nm, respectively, right y-scale: corresponding temperature variations of transverse thermoelectric conductivity  $\alpha_{xy}^{A}$ .

case and  $\lambda_{\rm Pt} \propto T^{-1,54}$  according to eq 1, the modified LSSE coefficient becomes  $^{22}$   $S_{\rm LSSE}^{\rm eff} = \frac{V_{\rm LSSE}}{\Delta T_{\rm eff} R_{\rm p} L_{\rm y}} \propto \left(\theta_{\rm SH}^{\rm Pt} \frac{G^{11}}{2\pi} \frac{k_{\rm B}}{D^{3/2}}\right) T^{3/2}.$  As shown in Figure 8a–c,  $S_{\rm LSSE}^{\rm eff}(T)$  varies as  $T^{1.41\pm0.12}$ ,  $T^{1.48\pm0.08}$ , and  $T^{1.49\pm0.1}$  for  $t_{\rm CoFeCrGa}=50$ , 95, and 200 nm, respectively, in the measured temperature range, which are in good agreement with the theory of thermally generated magnon-driven interfacial spin pumping mechanism.  $^{22,46,47}$ 

Now, let us understand the origin of ANE in our MgO/CoFeCrGa( $t_{\text{CoFeCrGa}}$ ) films. The transverse thermoelectric coefficient ( $S_{xy}$ ) is expressed as  $S_{xy} = \left[\frac{\alpha_{xy} - S_{xx}\alpha_{xy}}{\sigma_{xx}}\right]$ , where  $\sigma_{xx}$  and  $\sigma_{xy}$  are the longitudinal and transverse electrical conductivities, which are defined as  $S_{xy} = \left[\frac{\rho_{xx}}{(\rho_{xx})^2 + (\rho_{xy})^2}\right]$ 

and 
$$\sigma_{xy} = \left[\frac{-\rho_{xy}}{(\rho_{xx})^2 + (\rho_{xy})^2}\right]$$
, respectively. Also,  $\alpha_{xy}$  and  $S_{xx}$  are the

transverse thermoelectric conductivity and longitudinal Seebeck coefficient, which according to the Mott's relations

can be expressed as 
$$^{5,9}$$
  $\alpha_{xy} = \frac{\pi^2 k_B^2 T}{3\epsilon} \left(\frac{\partial \sigma_{xy}}{\partial E}\right)_{E=E_F}$  and  $S_{xx} = \frac{\pi^2 k_B^2 T}{3\epsilon \sigma_{xx}} \left(\frac{\partial \sigma_{xx}}{\partial E}\right)_{E=E_F}$ , respectively, where  $E_F$  is the Fermi energy. Since ANE and anomalous Hall effect (AHE) share the

energy. Since ANE and anomalous Hall effect (AHE) share the common physical origin and the AHE follows the power law connecting the anomalous Hall resistivity,  $\rho_{xy}^{AHE}$ , with the longitudinal electrical resistivity,  $\rho_{xx}$ , through the expression  $\rho_{xy}^{AHE} = \lambda M \rho_{xx}^{n}$ , where  $\lambda$  is the spin—orbit coupling constant and n is a constant exponent, the anomalous Nernst coefficient can be expressed as  $^{5,9}$ 

$$S_{xy}^{\text{ANE}} = \rho_{xx}^{n-1} \left[ \frac{\pi^2 k_{\text{B}}^2 T}{3e} \left( \frac{\partial \lambda}{\partial E} \right)_{E=E_{\text{F}}} - (n-1) \lambda S_{xx} \right]$$
 (6)

When n=1, the extrinsic skew scattering is the predominant mechanism for the anomalous Nernst/Hall transport, whereas n=2 indicates the intrinsic Berry curvature or the extrinsic side jump dominated anomalous Nernst/Hall transport. <sup>13</sup> Using the T-dependences of ANE voltage,  $V_{\rm ANE}(T)$  and  $\Delta T_{\rm eff}$ , we have estimated the T-dependence of the ANE coefficient,

$$S_{xy}^{\text{ANE}}(T) = \frac{V_{\text{ANE}}(T)}{\Delta T_{\text{eff}}(T)} \times \left(\frac{L_z}{L_y}\right)$$
, for the MgO/CoFeCrGa $(t_{\text{CoFeCrGa}})$ 

films, as shown in Figure 8d–f. Similar to the modified LSSE voltage,  $V_{\rm LSSE}^{\rm eff}(T)$ ,  $S_{xy}^{\rm ANE}(T)$  for the MgO/CoFeCrGa( $t_{\rm CoFeCrGa}$ ) films for all the three CoFeCrGa film thicknesses also increases as T decreases from room temperature and shows a maximum around 225 K below which it decreases rapidly with further decrease in temperature. Interestingly,  $S_{xy}^{\rm ANE}(T)$  for the MgO/CoFeCrGa (200 nm) film increases slowly with decreasing temperature from the room temperature, and the maximum around 225 K is much broader in contrast to the films with lower thicknesses.

Note that the values of  $S_{xy}^{\text{ANE}}$  for our MgO/CoFeCrGa- $(t_{\text{CoFeCrGa}})$  films are  $\approx 1.28$ , 1.86, and 4.9  $\mu$ V K<sup>-1</sup> at T=295 K and  $\approx 1.75$ , 2.63, and 5.1  $\mu$ V K<sup>-1</sup> at 225 K, for  $t_{\text{CoFeCrGa}}=50$ , 95, and 200 nm, respectively, which are nearly 2 orders of magnitude higher than that of the bulk polycrystalline sample of CoFeCrGa ( $\approx 0.018 \ \mu$ V K<sup>-1</sup> at 300 K)<sup>8</sup> and almost 3 orders of magnitude higher than that reported for the half-metallic ferromagnet La<sub>1-x</sub>Na<sub>x</sub>MnO<sub>3</sub> ( $\approx 4-5 \ \mu$ V K<sup>-1</sup>)<sup>6</sup> but comparable to that of the magnetic Weyl semimetal Co<sub>2</sub>MnGa thin films

( $\approx$ 2–3  $\mu$ V K<sup>-1</sup> at 300 K). See We fitted the  $S_{xy}^{ANE}(T)$  data in the temperature range 125 K  $\leq$  T  $\leq$  200 K for our MgO/ CoFeCrGa( $t_{\text{CoFeCrGa}}$ ) films using eq 6 considering  $\lambda$ ,  $\left(\frac{\partial \lambda}{\partial E}\right)_{E=E_{\text{E}}}$ 

and n as the fitting parameters. The best fit was obtained for n= 0.61  $\pm$  0.02, 0.68  $\pm$  0.06, and 0.87  $\pm$  0.05 for  $t_{\text{CoFeCrGa}}$  = 50, 95, and 200 nm, respectively, which implies that the origin of ANE in our MgO/CoFeCrGa( $t_{CoFeCrGa}$ ) films is dominated by the asymmetric skew scattering of charge carriers below 200 K.13 Note that we have also observed skew-scatteringdominated ANE in the bulk polycrystalline sample of CoFeCrGa,<sup>8</sup> for which  $n \approx 0.78$ .

Next, let us examine the temperature evolution of the anomalous off-diagonal thermoelectric conductivity,  $\alpha_{xv}^{A}$ . To determine  $\alpha_{xy}^{A}(T)$ , we have performed the Hall measurements on the MgO/CoFeCrGa( $t_{\text{CoFeCrGa}}$ ) films. Figure 9a-c presents the magnetic field dependence of Hall resistivity  $\rho_{xy}(H)$  of our MgO/CoFeCrGa( $t_{\text{CoFeCrGa}}$ ) films for  $t_{\text{CoFeCrGa}} = 50$ , 95, and 200 nm, respectively, recorded at few selected temperatures in the range 125 K  $\leq T \leq$  295 K. By subtracting the ordinary Hall effect (OHE) contribution from  $\rho_{xy}(H)$ , we determined the *T*dependence of the anomalous Hall resistivity  $\rho_{xy}^{AHE}(T)$ , which is shown in Figure S8. The left-y scales of Figure 9d-f exhibit the T-dependence of the anomalous Hall conductivity,

$$|\sigma_{xy}^{\text{AHE}}| = \left[\frac{\rho_{xy}^{\text{AHE}}}{(\rho_{xx})^2 + (\rho_{xy}^{\text{AHE}})^2}\right], \text{ of our MgO/CoFeCrGa}(t_{\text{CoFeCrGa}})$$

films for  $t_{\text{CoFeCrGa}}$  = 50, 95, and 200 nm, respectively. Note that  $|\sigma_{xy}^{\text{AHE}}(T)|$  for our MgO/CoFeCrGa( $t_{\text{CoFeCrGa}}$ ) films increases almost linearly with decreasing temperature, unlike UCo<sub>0.8</sub>Ru<sub>0.2</sub>Al for which  $|\sigma_{xy}^{AHE}|$  is nearly temperature independent at low temperatures. This implies that  $\sigma_{xy}^{AHE}$ for our MgO/CoFeCrGa (95 nm) film is strongly dependent on the scattering rate, which further supports that the extrinsic mechanisms (e.g., asymmetric skew scattering) dominate the transverse thermoelectric response of our sample at low temperatures.<sup>57</sup> However, it is evident that  $|\sigma_{xv}|^{AHE}$  changes nonmonotonically with the CoFeCrGa film thickness at low temperatures. Note that the value of  $|\sigma_{xy}^{AHE}|$  in our MgO/ CoFeCrGa films is nearly 2 orders of magnitude smaller than that reported for different topological ferromagnets, for example, UCo<sub>0.8</sub>Ru<sub>0.2</sub>Al, Co<sub>2</sub>MnGa, Co<sub>3</sub>Sn<sub>2</sub>S<sub>2</sub>, etc.<sup>57</sup> The value of  $|\sigma_{xy}^{AHE}| \approx 19,24$  and 15 S/cm at room temperature for the 50, 95, and 200 nm films, respectively, which are obviously very close to each other and comparable to those reported for CoFeCrGa thin films.<sup>33,35</sup> Therefore, the change in  $|\sigma_{xy}^{AHE}|$  with respect to thickness is within the measurement error range, at least at room temperature. In order to explain the nonmonotonous thickness dependence of  $|\sigma_{xy}^{AHE}|$  at low temperatures, let us recall that  $|\sigma_{xy}^{AHE}|$  is estimated using the

expression 
$$|\sigma_{xy}^{AHE}| = \left[\frac{\rho_{xy}^{AHE}}{(\rho_{xx})^2 + (\rho_{xy}^{AHE})^2}\right]$$
. As can be seen in Figure

9a-c,  $\rho_{xy}^{AHE}$  increases monotonically as a function of thickness at all temperatures, which is also evident from Figure S8. Therefore, the nonmonotonous thickness dependence of  $|\sigma_{rv}|^{AHE}$  may have arisen from the distinct temperature dependences of  $\sigma_{xx}$  in these films. As mentioned earlier, the SGS-based Huesler materials are extremely susceptible to disorder and defects, which cause significant changes in the electronic transport properties. We have already indicated that our MgO/CoFeCrGa films possess partial disorder/defects that gives rise to the slight difference in  $\sigma_{xx}(T)$  in the films with different thicknesses. Therefore, the nonmonotonous thickness

dependence of  $|\sigma_{xy}^{AHE}|$  at low temperatures in our MgO/ CoFeCrGa films might have been originated from a small amount of atomic disorder/defects in the films.

The right y-scale of Figure 9d-f illustrates the temperature variation of  $\alpha_{xy}^{A}$  of our MgO/CoFeCrGa( $t_{CoFeCrGa}$ ) films for  $t_{CoFeCrGa} = 50$ , 95, and 200 nm, respectively, which was obtained by incorporating the *T*-dependences of  $S_{xxy}$ ,  $S_{ANE}$ ,  $\rho_{xxy}$  and  $\rho_{xy}$  AHE in the expression  $\sigma_{xy}^{AHE} = \frac{S_{xy}^{ANE} - S_{xx} \sigma_{xy}^{AHE}}{\sigma_{xx}} = \frac{S_{xy}^{ANE} - S_{xx} \sigma_{xy}^{AHE}}{(\rho_{xx})^2 + (\rho_{xy}^{AHE})^2}$ . It is evident that

$$\alpha_{xy}^{A} = S_{xy}^{ANE} \sigma_{xx} + S_{xx} \sigma_{xy}^{AHE} = \left[ \frac{S_{xy}^{ANE} \rho_{xx} - S_{xx} \rho_{xy}^{AHE}}{(\rho_{xx})^2 + (\rho_{xx}^{AHE})^2} \right].$$
 It is evident that

 $\alpha_{xy}^{ANE}(T)$  for all the films shows a maximum around 225 K, similar to  $S_{xy}^{ANE}(T)$ . Note that similar to  $S_{xy}^{ANE}(T)$ ,  $\alpha_{xy}^{A}(T)$ for the MgO/CoFeCrGa (200 nm) film increases slowly with decreasing temperature from the room temperature, and the maximum around 225 K is much broader in contrast to the films with lower thicknesses. The values of  $\alpha_{xy}^{\ \ A}$  at room temperature (295 K) for our MgO/CoFeCrGa( $t_{\rm CoFeCrGa}$ ) films are 0.55, 0.77, and 1.4 A m<sup>-1</sup> K<sup>-1</sup> for  $t_{\rm CoFeCrGa}$  = 50, 95, and 200 nm, respectively, which are much smaller than that of noncentrosymmetric Kagome ferromagnet UCo<sub>0.8</sub>Ru<sub>0.2</sub>Al<sup>57</sup> ( $\approx$ 15 A m<sup>-1</sup> K<sup>-1</sup> at 40 K) and Co<sub>2</sub>MnGa single crystal<sup>10</sup> (≈7 A m<sup>-1</sup> K<sup>-1</sup> at 300 K) but closer to that of Co<sub>2</sub>MnGa thin films<sup>58</sup> ( $\approx$ 2 A m<sup>-1</sup> K<sup>-1</sup> at 300 K). Evidently,  $\alpha_{xy}^{-A}$  increases monotonically with thickness at all temperatures.

Next, we focus on the origin of the maximum in both  $S_{\rm LSSE}^{\rm eff}(T)$  and  $S_{xy}^{\rm ANE}(T)$  centered around 225 K. Note that the occurrence of maximum in both LSSE and ANE signals at the same temperature has been observed in other ferromagnetic metallic films, e.g., mixed valent manganites<sup>22</sup> and iron oxides. 50 The maximum in the temperature-dependent LSSE signal in the magnetically ordered state is commonly observed in different ferro- and ferrimagnets, for example, YIG, La<sub>0.7</sub>Ca<sub>0.3</sub>MnO<sub>3</sub>, etc., which originates as a consequence of the combined effects of boundary scattering and diffusive inelastic magnon-phonon or magnon-magnon scattering processes together with the reduction of magnon population at low temperatures. <sup>17,22,59</sup> In YIG, the maximum in the LSSE signal is thickness dependent; it shifts from ≈70 K for bulk YIG slab to  $\approx 200$  K for 1  $\mu$ m YIG film.<sup>17</sup> In ferromagnetic metals, extrinsic contributions arising from electron-magnon scattering contributes significantly to the anomalous Nernst thermopower.<sup>25</sup> In the presence of a temperature gradient and external magnetic field, magnons are excited in the bulk of a ferromagnetic material, and these thermally generated magnons transfer spin-angular momenta to the itinerant electrons via electron-magnon scattering as a result of which the itinerant electrons of the ferromagnetic layer get spin-polarized and contribute to the ANE. 25 Since the observed ANE in our MgO/CoFeCrGa( $t_{CoFeCrGa}$ ) films has dominating contribution from the extrinsic mechanism, the occurrence of maxima in  $S_{xy}^{\rm ANE}(T)$  around 225 K and the subsequent decrease in  $S_{xy}^{\rm ANE}$  in our MgO/CoFeCrGa( $t_{\rm CoFeCrGa}$ ) films can also be attributed to the diffusive inelastic magnon scatterings and reduced magnon population at low temperatures.<sup>25</sup> A decrease in the magnon population at low temperatures also reduces electron-magnon scattering which eventually diminishes the population of the spin-polarized itinerant electrons participating in the skew-scattering process. It is known that if  $\alpha_{xy}^{A}$  is dependent on the Berry curvature,  $S_{xy}^{ANE}$  is amplified by the presence of disorder. <sup>12</sup> However, the presence of defects does not influence the intrinsic contribution of ANE. As mentioned earlier, the atomic disorder and defects are negligible in our

MgO/CoFeCrGa films. Since  $S_{xy}^{\rm ANE}$  in our films is dominated by an extrinsic mechanism, the presence of a small amount of atomic disorder and defects can partially influence the ANE via electron-magnon scattering.

In the case of LSSE, the magnon propagation length  $\langle\langle\xi\rangle\rangle$  of the ferromagnetic material also plays a vital role in addition to the magnon population.  $\langle\xi\rangle$  signifies the critical length scale for thermally generated magnons to develop a spatial gradient of magnon accumulation inside a ferromagnetic film, which is one of the crucial factors that governs spin angular momentum transfer to the adjacent HM layer. A decrease in  $\langle\xi\rangle$  also suppresses the LSSE signal. It was theoretically shown that  $\langle\xi\rangle$  of a magnetic material with lattice constant  $a_0$  is related to the effective anisotropy constant  $(K_{\rm eff})$  and the Gilbert damping parameter  $(\alpha)$ , through the relation  $\xi = \frac{a_0}{2\alpha}$ .  $\sqrt{\frac{J_{\rm ex}}{2K_{\rm eff}}}$ , where  $J_{\rm ex}$  is the strength of the Heisenberg exchange interaction between nearest neighbors. Since  $K_{\rm eff} = \frac{1}{2}M_{\rm S}H_{\rm K}^{\rm eff}$ , the aforementioned expression can be written as  $\xi = \frac{a_0}{2\alpha}$ .  $\sqrt{\frac{J_{\rm ex}}{J_{\rm ex}}}$ 

. Thus,  $\langle \xi \rangle$  is inversely proportional to  $\alpha$  as well as the square root of  $(M_SH_K^{\text{eff}})$ . This implies that the T-evolution of  $\langle \xi \rangle$  is related to that of  $\alpha$ ,  $H_K^{\text{eff}}$  and  $M_S$ . As shown in Figure 3a,  $M_S$  for our MgO/CoFeCrGa (95 nm) film increases with decreasing temperature. Furthermore, H<sub>K</sub><sup>eff</sup> of our MgO/CoFeCrGa (95 nm) film for both IP and OOP configurations (both  $H_K^{IP}$  and  $H_{\rm K}^{\rm OOP}$ ) increases with decreasing temperature, and the increase is more rapid below ≈200 K compared to the temperature range of 200 K  $\leq T \leq$  300 K, as indicated in Figure 3f. Notably, a similar behavior of  $H_K^{\text{eff}}$  has been observed for the MgO/CoFeCrGa (200 nm) film (see Figure S2). Therefore, both  $H_{\rm K}^{\rm eff}$  and  $M_{\rm S}$  tend to suppress  $\langle \xi \rangle$  (and hence,  $S_{\rm LSSE}^{\rm eff}$ ) at low temperatures, especially below ≈200 K. To comprehend the role of  $\alpha$  in  $\langle \bar{\xi} \rangle$  and hence the LSSE signal at low temperatures, we have investigated the spin-dynamic properties of our MgO/CoFeCrGa (95 nm) and MgO/CoFeCrGa (95 nm)/Pt (5 nm) films by employing the broad-band ferromagnetic resonance (FMR) measurements.

**3.5.** Magnetization Dynamics and Gilbert Damping. Figure 10a,b displays the field derivative of microwave (MW) power absorption spectra  $\left(\frac{\mathrm{d}P}{\mathrm{d}H}\right)$  as a function of the IP DC magnetic field for various frequencies in the range  $4~\mathrm{GHz} \le f \le 18~\mathrm{GHz}$  recorded at  $T=250~\mathrm{K}$  for the MgO/CoFeCrGa (95 nm) and MgO/CoFeCrGa (95 nm)/Pt (5 nm) films, respectively. To extract the resonance field  $(H_{\mathrm{res}})$  and line width  $(\Delta H)$ , we fitted the  $\frac{\mathrm{d}P}{\mathrm{d}H}$  lineshapes with a linear combination of symmetric and antisymmetric Lorentzian function derivatives as  $^{61}$ 

$$\frac{dP}{dH} = P_{\text{Sym}} \frac{\frac{\Delta H}{2} (H_{\text{dc}} - H_{\text{res}})}{\left[ (H_{\text{dc}} - H_{\text{res}})^2 + \left(\frac{\Delta H}{2}\right)^2 \right]^2} + P_{\text{Asym}} \frac{\left(\frac{\Delta H}{2}\right)^2 - (H_{\text{dc}} - H_{\text{res}})^2}{\left[ (H_{\text{dc}} - H_{\text{res}})^2 + \left(\frac{\Delta H}{2}\right)^2 \right]^2} + P_0$$
(7)

where  $P_{\rm sym}$  and  $P_{\rm Asym}$  are the coefficients of the symmetric and antisymmetric Lorentzian derivatives, and  $P_0$  is a constant offset parameter. The fitted curves are represented by solid

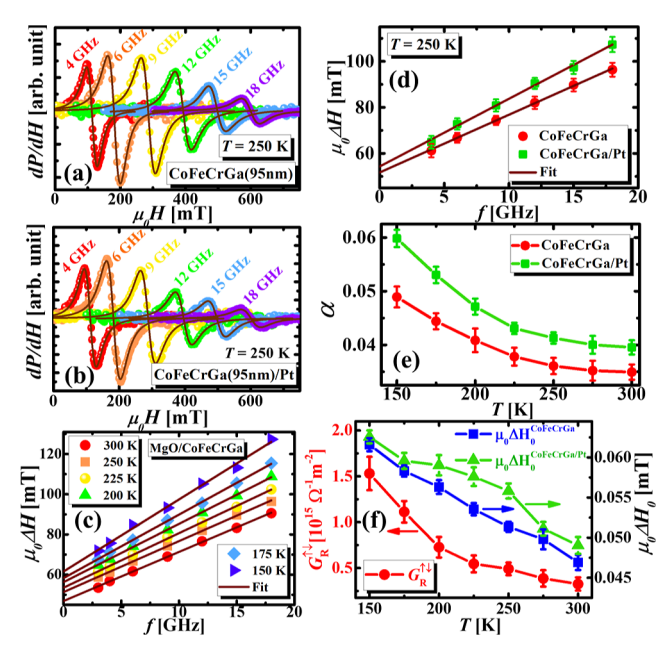


**Figure 10.** (a,b) Field derivative of microwave (MW) power absorption spectra  $\left(\frac{dP}{dH}\right)$  as a function of the IP DC magnetic field for various frequencies in the range 4 GHz ≤ f ≤ 18 GHz recorded at 250 K for the MgO/CoFeCrGa (95 nm) and MgO/CoFeCrGa (95 nm)/Pt (5 nm) films, respectively, fitted with eq 7. (c)  $\Delta H$ –f curves for the MgO/CoFeCrGa (95 nm) film at different temperatures fitted with  $\Delta H$ = $\Delta H_0$  +  $\frac{4\pi a}{\gamma \mu_0} f$ . (d) Comparison of the  $\Delta H$ –f curves for the MgO/CoFeCrGa (95 nm) and MgO/CoFeCrGa (95 nm)/Pt (5 nm) films recorded at 250 K. (e) Comparison of the temperature dependence of damping parameter  $\alpha$ (T) for the MgO/CoFeCrGa (95 nm) and MgO/CoFeCrGa (95 nm)/Pt (5 nm) films. (f) Right y-scale: temperature dependence of  $\Delta H_0$  for the MgO/CoFeCrGa (95 nm) and MgO/CoFeCrGa (95 nm)/Pt films, left y-scale: temperature dependence of the real component of the spin mixing conductance  $G_R^{\uparrow\downarrow}$  for the MgO/CoFeCrGa (95 nm)/Pt (5 nm) films.

lines in Figure 10a,b. To obtain the temperature evolution of the damping parameter,  $\alpha(T)$  for the MgO/CoFeCrGa (95 nm) and MgO/CoFeCrGa (95 nm)/Pt (5 nm) films, we have fitted the  $\Delta H - f$  curves with the expression 62  $\Delta H = \Delta H_0 + \frac{4\pi\alpha}{\gamma\mu_0} f$ , where  $\Delta H_0$  represents the inhomogeneous broadening,  $\frac{\gamma}{2\pi}=\frac{g_{\rm eff}\mu_{\rm B}}{\hbar}$  is the gyromagnetic ratio,  $\mu_{\rm B}$  is the Bohr magneton, and geff is the effective Landé g-factor. Figure 10c shows the  $\Delta H$ -f curves for the MgO/CoFeCrGa (95 nm) film at different temperatures fitted with the aforementioned expression. Clearly, the slope of the  $\Delta H - f$  curves increases with decreasing temperature, which implies increased  $\alpha$  at low temperatures. In Figure 10d, we compare the  $\Delta H-f$  curves for the MgO/CoFeCrGa (95 nm) and MgO/CoFeCrGa (95 nm)/Pt (5 nm) films recorded at T = 250 K. It is evident that  $\Delta H$  for MgO/CoFeCrGa (95 nm)/Pt (5 nm) is higher than that of MgO/CoFeCrGa (95 nm) for all the frequencies, which is because of the loss of spin angular momentum in the CoFeCrGa film as a result of spin pumping and can be

e x p r e s s e d a s  $[\Delta H_{\text{CoFeCrGa}/\text{Pt}} - \Delta H_{\text{CoFeCrGa}}] = G_{\text{R}}^{\uparrow\downarrow} \Big( \frac{g_{\text{eff}}\mu_{\text{B}}}{2\gamma M_{\text{s}}t_{\text{CoFeCrGa}}} \Big) f, \text{ where } G_{\text{R}}^{\uparrow\downarrow} \text{ is the real component of the interfacial spin mixing conductance } (G^{\uparrow\downarrow}). \text{ From the fits, we obtained } \alpha_{\text{CoFeCrGa}} = (3.6 \pm 0.2) \times 10^{-2} \text{ and } \alpha_{\text{CoFeCrGa}/\text{Pt}} = (4.12 \pm 0.1) \times 10^{-2} \text{ at } 250 \text{ K}$ 

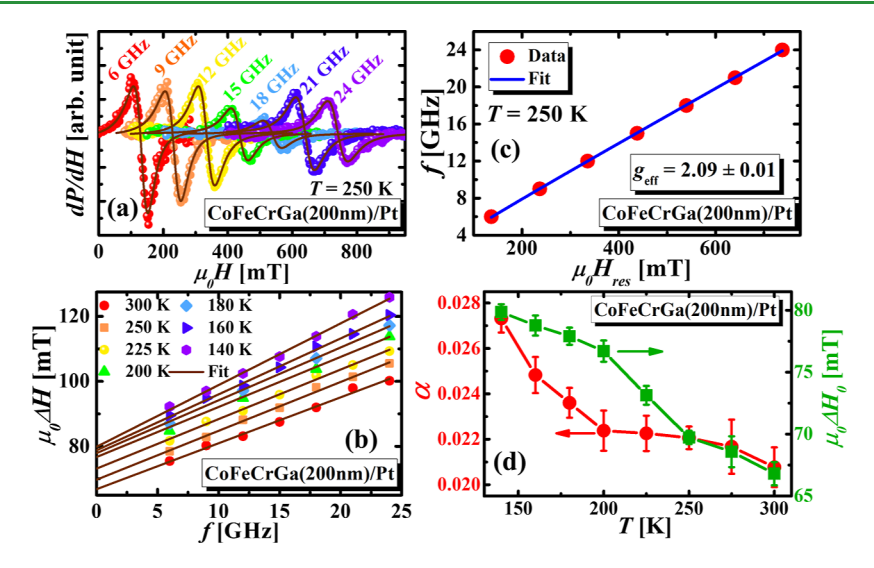


Figure 11. (a) Field derivative of  $\left(\frac{\mathrm{d}P}{\mathrm{d}H}\right)$  as a function of the IP DC magnetic field for various frequencies in the range: 4 GHz  $\leq f \leq$  18 GHz recorded at T=250 K for the MgO/CoFeCrGa (95 nm)/Pt fitted with eq 7. (b)  $\Delta H-f$  curves for the MgO/CoFeCrGa (200 nm)/Pt film at different temperatures fitted with  $\Delta H=\Delta H_0+\frac{4\pi\alpha}{\gamma\mu_0}f$ . (c) Fitting of the f vs the resonance field,  $H_{\rm res}$  using the Kittel's equation at T=250 K for the MgO/CoFeCrGa (200 nm)/Pt film. (d) Left y scale: temperature dependence of damping parameter  $\alpha(T)$  for the MgO/CoFeCrGa (200 nm)/Pt, and right y-scale: temperature dependence of  $\Delta H_0$  for the same.

for the MgO/CoFeCrGa (95 nm) and MgO/CoFeCrGa (95 nm)/Pt (5 nm) films, respectively. Clearly,  $\alpha_{\text{CoFeCrGa/Pt}} > \alpha_{\text{CoFeCrGa}}$ , which is caused by additional damping due to the spin pumping effect. In Figure 10e, we compare  $\alpha(T)$  for the MgO/CoFeCrGa (95 nm) and MgO/CoFeCrGa (95 nm)/Pt (5 nm) films. It is evident that  $\alpha_{\text{CoFeCrGa/Pt}} > \alpha_{\text{CoFeCrGa}}$  at all the temperatures, and both  $\alpha_{\text{CoFeCrGa/Pt}}$  and  $\alpha_{\text{CoFeCrGa}}$  increase with decreased temperature, especially below 225 K. Such increase in  $\alpha$  and  $\Delta H$  at low temperatures can be primarily attributed to the impurity relaxation mechanisms. Since  $\xi \propto \frac{1}{\alpha}$ , an increase in  $\alpha$  at low temperatures gives rise to a decrease in  $\langle \xi \rangle$  and hence the LSSE signal.

The increases in  $\Delta H_0$  at low temperatures for both MgO/ CoFeCrGa (95 nm) and MgO/CoFeCrGa (95 nm)/Pt (5 nm) films (see the right y-scale of Figure 10f) also support the occurrence of impurity relaxation at low temperatures.<sup>67</sup> The presence of a small amount of atomic disorder and defects in our MgO/CoFeCrGa films promotes impurity relaxation and contributes toward low temperature increase in  $\alpha$  and hence leads to the decrease in the LSSE signal at low temperatures. To have a quantitative understanding of the T-evolution of spin pumping efficiency in the MgO/CoFeCrGa(95 nm)/Pt(5 nm) film, we estimated  $G_{\mathbb{R}}^{\uparrow\downarrow}$  using the expression<sup>68</sup>  $G_R^{\uparrow\downarrow} = \left(\frac{2e^2}{\hbar}\right) \left(\frac{2\pi M_{\rm S} t_{\rm CoFeCrGa}}{g_{\rm eff} \mu_{\rm B}}\right) [\alpha_{
m CoFeCrGa/Pt} - \alpha_{
m CoFeCrGa}], \quad {
m where}$  $G_0 = \left(\frac{2e^2}{h}\right)$  is the conductance quantum, and found that  $G_R^{\uparrow\downarrow}$  $pprox 3.25 \times 10^{14} \ \Omega^{-1} \ m^{-2}$  at 300 K, which is close to  $G_{\rm R}^{\uparrow\downarrow} = 7.5 \times 10^{14} \ \Omega^{-1} \ m^{-2}$  in YIG/Pt<sup>69</sup> and  $G_{\rm R}^{\uparrow\downarrow} = 5.7 \times 10^{14} \ \Omega^{-1} \ m^{-2}$  in TmIG/Pt bilayers.<sup>68</sup> As shown in Figure 10d,  $G_R^{\uparrow\downarrow}$  for the MgO/CoFeCrGa (95 nm)/Pt (5 nm) film increases with decreasing temperature, which is consistent with the phenomenological expression,  $^{70}$   $G_{\rm R}^{\uparrow\downarrow}$   $\propto$   $(T_{\rm C}-T)$ , where  $T_{\rm C}$ = Curie temperature. Furthermore, to confirm the aforementioned behavior of the temperature evolution of  $\alpha$ , we have repeated the broad-band FMR measurements on the MgO/ CoFeCrGa (95 nm)/Pt (5 nm) film. Figure 11a display the

magnetic field dependence of the  $\left(\frac{\mathrm{d}^P}{\mathrm{d}H}\right)$  lineshapes in the range:  $6~\mathrm{GHz} \leq f \leq 24~\mathrm{GHz}$  recorded at  $T=250~\mathrm{K}$  for the MgO/CoFeCrGa (200 nm)/Pt film, fitted with eq 7. To obtain the temperature evolution of the damping parameter,  $\alpha(T)$ , we have fitted the  $\Delta H-f$  curves at different temperatures in the range of  $140~\mathrm{K} \leq T \leq 300~\mathrm{K}$  with the expression  $^{62}$   $\Delta H=\Delta H_0+\frac{4\pi\alpha}{\gamma\mu_0}f$ , as shown in Figure 11b. Evidently, the slope of the  $\Delta H-f$  curves increases with decreasing temperature, which implies increased  $\alpha$  at low temperatures. Moreover, in Figure 11c, we show the fitting of the  $f-H_{\mathrm{res}}$  curves at  $T=250~\mathrm{K}$  using Kittel's equation for magnetic thin films with IP magnetic field,  $^{64}$  which is expressed as  $f=\frac{\gamma\mu_0}{2\pi}\sqrt{H_{\mathrm{res}}(H_{\mathrm{res}}+M_{\mathrm{eff}})}$ , where  $M_{\mathrm{eff}}$  is the effective magnetization

The estimated value of  $g_{\rm eff}=(2.09\pm0.01)$  at 250 K for the MgO/CoFeCrGa (200 nm)/Pt (5 nm) film, which is slightly higher than the free electron value ( $g_{\rm eff}=2.002$ ). Note that  $g_{\rm eff}=(2.046\pm0.01)$  and (2.048  $\pm$  0.02) for the MgO/CoFeCrGa (95 nm) and MgO/CoFeCrGa (95 nm)/Pt (5 nm) films, respectively, at 250 K. Finally,  $\alpha(T)$  for the MgO/CoFeCrGa (95 nm)/Pt (5 nm) film is shown on the left *y*-axis of Figure 11d. It is evident that  $\alpha(T)$  increases with decreasing temperature, especially below 225 K similar to what we have observed for the MgO/CoFeCrGa (95 nm) and MgO/CoFeCrGa (95 nm)/Pt (5 nm) films. This observation further confirms the contribution of  $\alpha$  toward the observed decrease in the LSSE signal in the CoFeCrGa films below the temperature range of 200–225 K.

#### 4. CONCLUSIONS

In summary, we present a comprehensive investigation of the temperature ANE and intrinsic longitudinal spin Seebeck effect (LSSE) in the quaternary Heusler alloy-based SGS thin films of CoFeCrGa grown on MgO substrates. We found that the anomalous Nernst coefficient for the MgO/CoFeCrGa (95

nm) film is  $\approx 1.86 \,\mu\text{V K}^{-1}$  at room temperature, which is much higher than the bulk polycrystalline sample of CoFeCrGa  $(\approx 0.018 \ \mu V \ K^{-1} \ at \ 300 \ K)$  but comparable to that of the magnetic Weyl semimetal Co₂MnGa thin films (≈1.86 µV K<sup>-</sup> at 300 K). Furthermore, the LSSE coefficient for our MgO/ CoFeCrGa (95 nm)/Pt (5 nm) heterostructure is ≈ 20.5 nV  $K^{-1}$   $\Omega^{-1}$  at 295 K, which is twice larger than that of the halfmetallic ferromagnetic La<sub>0.7</sub>Sr<sub>0.3</sub>MnO<sub>3</sub> thin films (≈9 nV K<sup>-1</sup>  $\Omega^{-1}$  at room temperature). We have shown that both ANE and LSSE coefficients follow identical temperature dependences and exhibit a maximum ≈225 K which is understood as the combined effects of inelastic magnon scatterings and reduced magnon population at low temperatures. Our analyses not only indicated that the extrinsic skew scattering is the dominating mechanism for ANE in these films but also provided critical insights into the functional form of the observed temperaturedependent LSSE at low temperatures. Furthermore, by employing radio frequency transverse susceptibility and broad-band ferromagnetic resonance in combination with the LSSE measurements, we have established a correlation among the observed LSSE signal, magnetic anisotropy, and Gilbert damping of the CoFeCrGa thin films which will be beneficial for fabricating tunable and highly efficient spin caloritronic nanodevices. We believe that our findings will also attract the attention of materials science and spintronics community for further exploration of different Heusler alloy-based magnetic thin films and heterostructures coexhibiting multiple thermospin effects with promising efficiencies.

#### ASSOCIATED CONTENT

### **Data Availability Statement**

The data that support the findings of this study are available from the corresponding author upon reasonable request.

### Supporting Information

The Supporting Information is available free of charge at https://pubs.acs.org/doi/10.1021/acsami.3c12342.

Magnetometry, temperature dependence of electrical resistivity, magnetic field and temperature dependences of transverse susceptibility, magnetic field dependence of ANE and LSSE voltages for the MgO/CoFeCrGa (200 nm), and MgO/CoFeCrGa (50 nm) films (PDF)

#### AUTHOR INFORMATION

## **Corresponding Authors**

Amit Chanda — Department of Physics, University of South Florida, Tampa, Florida 33620, United States; orcid.org/0000-0001-9681-0312; Email: achanda@usf.edu

Hariharan Srikanth — Department of Physics, University of South Florida, Tampa, Florida 33620, United States; orcid.org/0000-0002-2541-7000; Email: sharihar@usf.edu

#### **Authors**

Deepika Rani — Physics Department, Indian Institute of Technology Delhi, New Delhi 110016, India

Derick DeTellem - Department of Physics, University of South Florida, Tampa, Florida 33620, United States

Noha Alzahrani – Department of Physics, University of South Florida, Tampa, Florida 33620, United States

Dario A. Arena — Department of Physics, University of South Florida, Tampa, Florida 33620, United States; orcid.org/0000-0001-7463-6472

Sarath Witanachchi — Department of Physics, University of South Florida, Tampa, Florida 33620, United States

Ratnamala Chatterjee – Physics Department, Indian Institute of Technology Delhi, New Delhi 110016, India

Manh-Huong Phan — Department of Physics, University of South Florida, Tampa, Florida 33620, United States;
orcid.org/0000-0002-6270-8990

Complete contact information is available at: https://pubs.acs.org/10.1021/acsami.3c12342

#### **Notes**

The authors declare no competing financial interest.

#### ACKNOWLEDGMENTS

H.S. and M.H.P. acknowledge the support from the US Department of Energy, Office of Basic Energy Sciences, Division of Materials Science and Engineering, under Award no. DE-FG02-07ER46438. H.S. thanks the Alexander von Humboldt foundation for a research award and also acknowledges a visiting professorship at IIT Bombay. D.A.A. acknowledges the support of the National Science Foundation under grant no. ECCS-1952957. D.D. and R.C. acknowledge the financial assistance received from the DST Nanomission project (DST/NM/TUE/QM-11/2019).

#### REFERENCES

- (1) Bauer, G. E. W.; Saitoh, E.; Van Wees, B. J. Spin Caloritronics. *Nat. Mater.* **2012**, *11* (5), 391–399.
- (2) Sakai, A.; Mizuta, Y. P.; Nugroho, A. A.; Sihombing, R.; Koretsune, T.; Suzuki, M.-T.; Takemori, N.; Ishii, R.; Nishio-Hamane, D.; Arita, R.; et al. Giant anomalous Nernst effect and quantum-critical scaling in a ferromagnetic semimetal. *Nat. Phys.* **2018**, *14* (11), 1119–1124.
- (3) Uchida, K.; Adachi, H.; Ota, T.; Nakayama, H.; Maekawa, S.; Saitoh, E. Observation of Longitudinal Spin-Seebeck Effect in Magnetic Insulators. *Appl. Phys. Lett.* **2010**, *97* (17), 172505.
- (4) Daimon, S.; Iguchi, R.; Hioki, T.; Saitoh, E.; Uchida, K. Thermal Imaging of Spin Peltier Effect. *Nat. Commun.* **2016**, *7* (1), 13754.
- (5) Pu, Y.; Chiba, D.; Matsukura, F.; Ohno, H.; Shi, J. Mott Relation for Anomalous Hall and Nernst Effects in Ga 1- x Mn x As Ferromagnetic Semiconductors. *Phys. Rev. Lett.* **2008**, *101* (11), 117208.
- (6) Ghosh, A.; Das, R.; Mahendiran, R. Skew Scattering Dominated Anomalous Nernst Effect in La1-x Na x MnO3. *J. Appl. Phys.* **2019**, 125 (15), 153902.
- (7) Ghosh, A.; Chanda, A.; Mahendiran, R. Anomalous Nernst Effect in Pr0. 5Sr0. 5CoO3. AIP Adv. 2021, 11 (3), 35031.
- (8) Chanda, A.; Rani, D.; Nag, J.; Alam, A.; Suresh, K. G.; Phan, M. H.; Srikanth, H. Emergence of Asymmetric Skew-Scattering Dominated Anomalous Nernst Effect in the Spin Gapless Semiconductors Co 1+ x Fe 1- x CrGa. *Phys. Rev. B* **2022**, *106* (13), 134416.
- (9) Ramos, R.; Aguirre, M. H.; Anadón, A.; Blasco, J.; Lucas, I.; Uchida, K.; Algarabel, P. A.; Morellón, L.; Saitoh, E.; Ibarra, M. R. Anomalous Nernst Effect of Fe3 O 4 Single Crystal. *Phys. Rev. B: Condens. Matter Mater. Phys.* **2014**, *90* (5), 54422.
- (10) Guin, S. N.; Manna, K.; Noky, J.; Watzman, S. J.; Fu, C.; Kumar, N.; Schnelle, W.; Shekhar, C.; Sun, Y.; Gooth, J.; et al. Anomalous Nernst Effect beyond the Magnetization Scaling Relation in the Ferromagnetic Heusler Compound Co2MnGa. *NPG Asia Mater.* **2019**, *11* (1), 16.
- (11) Yang, H.; You, W.; Wang, J.; Huang, J.; Xi, C.; Xu, X.; Cao, C.; Tian, M.; Xu, Z.-A.; Dai, J.; et al. Giant Anomalous Nernst Effect in the Magnetic Weyl Semimetal Co 3 Sn 2 S 2. *Phys. Rev. Mater.* **2020**, 4 (2), 24202.

- (12) Ding, L.; Koo, J.; Xu, L.; Li, X.; Lu, X.; Zhao, L.; Wang, Q.; Yin, Q.; Lei, H.; Yan, B.; et al. Intrinsic Anomalous Nernst Effect Amplified by Disorder in a Half-Metallic Semimetal. *Phys. Rev. X* **2019**, 9 (4), 41061.
- (13) Nagaosa, N.; Sinova, J.; Onoda, S.; MacDonald, A. H.; Ong, N. P. Anomalous Hall Effect. *Rev. Mod. Phys.* **2010**, 82 (2), 1539–1592.
- (14) Ghosh, A.; De, A.; Nair, S. Large Anomalous Nernst Effect across the Magneto-Structural Transition in a Bulk Ni-Co-Mn-Sn Full Heusler Alloy. *Appl. Phys. Lett.* **2018**, *113* (26), 262405.
- (15) Chanda, A.; Holzmann, C.; Schulz, N.; Seyd, J.; Albrecht, M.; Phan, M.-H.; Srikanth, H. Scaling of the Thermally Induced Sign Inversion of Longitudinal Spin Seebeck Effect in a Compensated Ferrimagnet: Role of Magnetic Anisotropy. *Adv. Funct. Mater.* **2022**, 32 (9), 2109170.
- (16) Kehlberger, A.; Ritzmann, U.; Hinzke, D.; Guo, E.-J.; Cramer, J.; Jakob, G.; Onbasli, M. C.; Kim, D. H.; Ross, C. A.; Jungfleisch, M. B.; et al. Length Scale of the Spin Seebeck Effect. *Phys. Rev. Lett.* **2015**, 115 (9), 096602.
- (17) Guo, E.-J.; Cramer, J.; Kehlberger, A.; Ferguson, C. A.; MacLaren, D. A.; Jakob, G.; Kläui, M. Influence of Thickness and Interface on the Low-Temperature Enhancement of the Spin Seebeck Effect in YIG Films. *Phys. Rev. X* **2016**, *6* (3), 031012.
- (18) Ritzmann, U.; Hinzke, D.; Kehlberger, A.; Guo, E.-J.; Kläui, M.; Nowak, U. Magnetic Field Control of the Spin Seebeck Effect. *Phys. Rev. B: Condens. Matter Mater. Phys.* **2015**, 92 (17), 174411.
- (19) Xu, J.; He, J.; Zhou, J.-S.; Qu, D.; Huang, S.-Y.; Chien, C. L. Observation of Vector Spin Seebeck Effect in a Noncollinear Antiferromagnet. *Phys. Rev. Lett.* **2022**, *129* (11), 117202.
- (20) Uchida, K.; Takahashi, S.; Harii, K.; Ieda, J.; Koshibae, W.; Ando, K.; Maekawa, S.; Saitoh, E. Observation of the Spin Seebeck Effect. *Nature* **2008**, *455* (7214), 778–781.
- (21) Ramos, R.; Kikkawa, T.; Uchida, K.; Adachi, H.; Lucas, I.; Aguirre, M. H.; Algarabel, P.; Morellón, L.; Maekawa, S.; Saitoh, E.; et al. Observation of the Spin Seebeck Effect in Epitaxial Fe3O4 Thin Films. *Appl. Phys. Lett.* **2013**, *102* (7), 72413.
- (22) De, A.; Ghosh, A.; Mandal, R.; Ogale, S.; Nair, S. Temperature Dependence of the Spin Seebeck Effect in a Mixed Valent Manganite. *Phys. Rev. Lett.* **2020**, *124* (1), 017203.
- (23) Wu, B. W.; Luo, G. Y.; Lin, J. G.; Huang, S. Y. Longitudinal Spin Seebeck Effect in a Half-Metallic L a 0.7 S r 0.3 Mn O 3 Film. *Phys. Rev. B* **2017**, *96* (6), 060402.
- (24) Jaworski, C. M.; Yang, J.; Mack, S.; Awschalom, D. D.; Heremans, J. P.; Myers, R. C. Observation of the Spin-Seebeck Effect in a Ferromagnetic Semiconductor. *Nat. Mater.* **2010**, *9* (11), 898–903.
- (25) He, B.; Şahin, C.; Boona, S. R.; Sales, B. C.; Pan, Y.; Felser, C.; Flatté, M. E.; Heremans, J. P. Large Magnon-Induced Anomalous Nernst Conductivity in Single-Crystal MnBi. *Joule* **2021**, *5* (11), 3057–3067.
- (26) Ouardi, S.; Fecher, G. H.; Felser, C.; Kübler, J. Realization of Spin Gapless Semiconductors: The Heusler Compound Mn 2 CoAl. *Phys. Rev. Lett.* **2013**, *110* (10), 100401.
- (27) Bainsla, L.; Mallick, A. I.; Raja, M. M.; Coelho, A. A.; Nigam, A. K.; Johnson, D. D.; Alam, A.; Suresh, K. G. Origin of Spin Gapless Semiconductor Behavior in CoFeCrGa: Theory and Experiment. *Phys. Rev. B: Condens. Matter Mater. Phys.* **2015**, 92 (4), 045201.
- (28) Rani, D.; Bainsla, L.; Bainsla, L.; Suresh, K. G.; Alam, A.; et al. Spin-Gapless Semiconducting Nature of Co-Rich Co 1+ x Fe 1- x CrGa. *Phys. Rev. B* **2019**, *99* (10), 104429.
- (29) Han, J.; Feng, Y.; Yao, K.; Gao, G. Y. Spin Transport Properties Based on Spin Gapless Semiconductor CoFeMnSi. *Appl. Phys. Lett.* **2017**, *111* (13), 132402.
- (30) Chanda, A.; Shoup, J. E.; Schulz, N.; Arena, D. A.; Srikanth, H. Tunable Competing Magnetic Anisotropies and Spin Reconfigurations in Ferrimagnetic Fe 100- x Gd x Alloy Films. *Phys. Rev. B* **2021**, 104 (9), 094404.
- (31) Chanda, A.; Nag, J.; Alam, A.; Suresh, K. G.; Phan, M.-H.; Srikanth, H. Intrinsic Berry Curvature Driven Anomalous Nernst

- Thermopower in the Semimetallic Heusler Alloy CoFeVSb. *Phys. Rev. B* **2023**, *107* (22), L220403.
- (32) Alijani, V.; Ouardi, S.; Fecher, G. H.; Winterlik, J.; Naghavi, S. S.; Kozina, X.; Stryganyuk, G.; Felser, C.; Ikenaga, E.; Yamashita, Y.; et al. Electronic, Structural, and Magnetic Properties of the Half-Metallic Ferromagnetic Quaternary Heusler Compounds CoFeMn Z (Z= Al, Ga, Si, Ge). *Phys. Rev. B: Condens. Matter Mater. Phys.* **2011**, 84 (22), 224416.
- (33) Mishra, V.; Kumar, A.; Pandey, L.; Gupta, N. K.; Hait, S.; Barwal, V.; Sharma, N.; Kumar, N.; Chandra, S.; Chaudhary, S. Disordered Spin Gapless Semiconducting CoFeCrGa Heusler Alloy Thin Films on Si (100): Experiment and Theory. *Nanoscale* **2023**, *15* (1), 337–349.
- (34) Kazakova, O.; Puttock, R.; Barton, C.; Corte-León, H.; Jaafar, M.; Neu, V.; Asenjo, A. Frontiers of Magnetic Force Microscopy. *J. Appl. Phys.* **2019**, *125* (6), 60901.
- (35) Rani, D.; Pandey, D. K.; Kimura, Y.; Umetsu, R. Y.; Chatterjee, R. Structural, Magnetic, and Transport Properties of Epitaxial Thin Films of Equiatomic Quaternary CoFeCrGa Heusler Alloy. *J. Appl. Phys.* **2022**, *132* (19), 193907.
- (36) Kushwaha, V. K.; Rani, J.; Tulapurkar, A.; Tomy, C. V. Possible Spin Gapless Semiconductor Type Behaviour in CoFeMnSi Epitaxial Thin Films. *Appl. Phys. Lett.* **2017**, *111* (15), 152407.
- (37) Kharel, P.; Zhang, W.; Skomski, R.; Valloppilly, S.; Huh, Y.; Fuglsby, R.; Gilbert, S.; Sellmyer, D. J. Magnetism, Electron Transport and Effect of Disorder in CoFeCrAl. *J. Phys. D Appl. Phys.* **2015**, 48 (24), 245002.
- (38) Pradines, B.; Arras, R.; Abdallah, I.; Biziere, N.; Calmels, L. First-Principles Calculation of the Effects of Partial Alloy Disorder on the Static and Dynamic Magnetic Properties of Co 2 MnSi. *Phys. Rev. B* **2017**, *95* (9), 094425.
- (39) Biswas, S.; Chaudhuri, S.; Kander, N.; Mitra, S.; Guchhait, S.; Das, A. K. Effect of Disorder and Strain on Spin Polarization of a Co2FeSi Heusler Alloy. *ACS Appl. Electron. Mater.* **2021**, 3 (10), 4522–4534.
- (40) Xin, F.; You, C.; Fu, H.; Ma, L.; Cheng, Z.; Tian, N. Mechanically Tuning Magnetism and Transport Property in Spin Gapless Semiconductor CoFeMnSi Flexible Thin Film. *J. Alloys Compd.* **2020**, *813*, 152207.
- (41) Jamer, M. E.; Assaf, B. A.; Devakul, T.; Heiman, D. Magnetic and Transport Properties of Mn2CoAl Oriented Films. *Appl. Phys. Lett.* **2013**, *103* (14), 142403.
- (42) Xu, G. Z.; Du, Y.; Zhang, X. M.; Zhang, H. G.; Liu, E. K.; Wang, W. H.; Wu, G. H. Magneto-Transport Properties of Oriented Mn2CoAl Films Sputtered on Thermally Oxidized Si Substrates. *Appl. Phys. Lett.* **2014**, *104* (24), 242408.
- (43) Khosla, R. P.; Fischer, J. R. Magnetoresistance in Degenerate CdS: Localized Magnetic Moments. *Phys. Rev. B: Solid State* **1970**, 2 (10), 4084–4097.
- (44) Peters, J. A.; Parashar, N. D.; Rangaraju, N.; Wessels, B. W. Magnetotransport Properties of InMnSb Magnetic Semiconductor Thin Films. *Phys. Rev. B: Condens. Matter Mater. Phys.* **2010**, 82 (20), 205207.
- (45) Stephen, G. M.; Lane, C.; Buda, G.; Graf, D.; Kaprzyk, S.; Barbiellini, B.; Bansil, A.; Heiman, D. Electrical and Magnetic Properties of Thin Films of the Spin-Filter Material CrVTiAl. *Phys. Rev. B* **2019**, 99 (22), 224207.
- (46) Weiler, M.; Althammer, M.; Schreier, M.; Lotze, J.; Pernpeintner, M.; Meyer, S.; Huebl, H.; Gross, R.; Kamra, A.; Xiao, J.; et al. Experimental Test of the Spin Mixing Interface Conductivity Concept. *Phys. Rev. Lett.* **2013**, *111* (17), 176601.
- (47) Xiao, J.; Bauer, G. E. W.; Uchida, K.; Saitoh, E.; Maekawa, S. Theory of Magnon-Driven Spin Seebeck Effect. *Phys. Rev. B: Condens. Matter Mater. Phys.* **2010**, *81* (21), 214418.
- (48) Rezende, S. M.; Rodríguez-Suárez, R. L.; Cunha, R. O.; Rodrigues, A. R.; Machado, F. L. A.; Fonseca Guerra, G. A.; Lopez Ortiz, J. C.; Azevedo, A. Magnon Spin-Current Theory for the Longitudinal Spin-Seebeck Effect. *Phys. Rev. B: Condens. Matter Mater. Phys.* **2014**, 89 (1), 14416.

- (49) Bougiatioti, P.; Klewe, C.; Meier, D.; Manos, O.; Kuschel, O.; Wollschläger, J.; Bouchenoire, L.; Brown, S. D.; Schmalhorst, J.-M.; Reiss, G.; et al. Quantitative Disentanglement of the Spin Seebeck, Proximity-Induced, and Ferromagnetic-Induced Anomalous Nernst Effect in Normal-Metal-Ferromagnet Bilayers. *Phys. Rev. Lett.* **2017**, 119 (22), 227205.
- (50) Chanda, A.; DeTellem, D.; Hai Pham, Y. T.; Shoup, J. E.; Duong, A. T.; Das, R.; Cho, S.; Voronine, D. V.; Trinh, M. T.; Arena, D. A.; et al. Spin Seebeck Effect in Iron Oxide Thin Films: Effects of Phase Transition, Phase Coexistence, And Surface Magnetism. ACS Appl. Mater. Interfaces 2022, 14 (11), 13468–13479.
- (51) Jiménez-Cavero, P.; Lucas, I.; Bugallo, D.; López-Bueno, C.; Ramos, R.; Algarabel, P. A.; Ibarra, M. R.; Rivadulla, F.; Morellón, L. Quantification of the Interfacial and Bulk Contributions to the Longitudinal Spin Seebeck Effect. *Appl. Phys. Lett.* **2021**, *118* (9), 92404.
- (52) Ashworth, T.; Loomer, J. E.; Kreitman, M. M. Thermal Conductivity of Nylons and Apiezon Greases. In *Advances in Cryogenic Engineering*; Springer, 1973; pp 271–279.
- (53) Grimvall, G. Thermophysical Properties of Materials; Elsevier, 1999.
- (54) Marmion, S. R.; Ali, M.; McLaren, M.; Williams, D. A.; Hickey, B. J. Temperature Dependence of Spin Hall Magnetoresistance in Thin YIG/Pt Films. *Phys. Rev. B: Condens. Matter Mater. Phys.* **2014**, 89 (22), 220404.
- (55) Xu, J.; Phelan, W. A.; Chien, C.-L. Large Anomalous Nernst Effect in a van Der Waals Ferromagnet Fe3GeTe2. *Nano Lett.* **2019**, 19 (11), 8250–8254.
- (56) Kim, M.; Park, S. J.; Jin, H. Enhancing the Spin Seebeck Effect by Controlling Interface Condition in Pt/Polycrystalline Nickel Ferrite Slabs. *J. Appl. Phys.* **2020**, *127* (8), 85105.
- (57) Asaba, T.; Ivanov, V.; Thomas, S. M.; Savrasov, S. Y.; Thompson, J. D.; Bauer, E. D.; Ronning, F. Colossal Anomalous Nernst Effect in a Correlated Noncentrosymmetric Kagome Ferromagnet. *Sci. Adv.* **2021**, *7* (13), No. eabf1467.
- (58) Park, G.-H.; Reichlova, H.; Schlitz, R.; Lammel, M.; Markou, A.; Swekis, P.; Ritzinger, P.; Kriegner, D.; Noky, J.; Gayles, J.; et al. Thickness Dependence of the Anomalous Nernst Effect and the Mott Relation of Weyl Semimetal Co 2 MnGa Thin Films. *Phys. Rev. B* **2020**, *101* (6), 60406.
- (59) Jin, H.; Boona, S. R.; Yang, Z.; Myers, R. C.; Heremans, J. P. Effect of the Magnon Dispersion on the Longitudinal Spin Seebeck Effect in Yttrium Iron Garnets. *Phys. Rev. B: Condens. Matter Mater. Phys.* **2015**, 92 (5), 054436.
- (60) Ritzmann, U.; Hinzke, D.; Nowak, U. Propagation of Thermally Induced Magnonic Spin Currents. *Phys. Rev. B: Condens. Matter Mater. Phys.* **2014**, 89 (2), 024409.
- (61) Dürrenfeld, P.; Gerhard, F.; Chico, J.; Dumas, R. K.; Ranjbar, M.; Bergman, A.; Bergqvist, L.; Delin, A.; Gould, C.; Molenkamp, L. W.; et al. Tunable damping, saturation magnetization, and exchange stiffness of half-Heusler NiMnSb thin films. *Phys. Rev. B: Condens. Matter Mater. Phys.* **2015**, 92 (21), 214424.
- (62) Nembach, H. T.; Silva, T. J.; Shaw, J. M.; Schneider, M. L.; Carey, M. J.; Maat, S.; Childress, J. R. Perpendicular Ferromagnetic Resonance Measurements of Damping and Land e G- Factor in Sputtered (Co 2 Mn) 1- x Ge x Thin Films. *Phys. Rev. B: Condens. Matter Mater. Phys.* **2011**, 84 (5), 054424.
- (63) Mosendz, O.; Pearson, J. E.; Fradin, F. Y.; Bauer, G. E. W.; Bader, S. D.; Hoffmann, A. Quantifying Spin Hall Angles from Spin Pumping: Experiments and Theory. *Phys. Rev. Lett.* **2010**, *104* (4), 046601.
- (64) Jermain, C. L.; Aradhya, S. V.; Reynolds, N. D.; Buhrman, R. A.; Brangham, J. T.; Page, M. R.; Hammel, P. C.; Yang, F. Y.; Ralph, D. C. Increased Low-Temperature Damping in Yttrium Iron Garnet Thin Films. *Phys. Rev. B* **2017**, *95* (17), 174411.
- (65) Seiden, P. E. Ferrimagnetic Resonance Relaxation in Rare-Earth Iron Garnets. *Phys. Rev.* **1964**, *133* (3A), A728–A736.
- (66) Vilela, G. L. S.; Abrao, J. E.; Santos, E.; Yao, Y.; Mendes, J. B. S.; Rodríguez-Suárez, R. L.; Rezende, S. M.; Han, W.; Azevedo, A.;

- Moodera, J. S. Magnon-Mediated Spin Currents in Tm3Fe5O12/Pt with Perpendicular Magnetic Anisotropy. *Appl. Phys. Lett.* **2020**, *117* (12), 122412.
- (67) Guo, S.; McCullian, B.; Chris Hammel, P.; Yang, F. Low Damping at Few-K Temperatures in Y3Fe5O12 Epitaxial Films Isolated from Gd3Ga5O12 Substrate Using a Diamagnetic Y3Sc2. 5Al2. 5O12 Spacer. J. Magn. Magn. Mater. 2022, 562, 169795.
- (68) Crossley, S.; Quindeau, A.; Swartz, A. G.; Rosenberg, E. R.; Beran, L.; Avci, C. O.; Hikita, Y.; Ross, C. A.; Hwang, H. Y. Ferromagnetic Resonance of Perpendicularly Magnetized Tm3Fe5O12/Pt Heterostructures. *Appl. Phys. Lett.* **2019**, *115* (17), 172402.
- (69) Haertinger, M.; Back, C. H.; Lotze, J.; Weiler, M.; Geprägs, S.; Huebl, H.; Goennenwein, S. T. B.; Woltersdorf, G. Spin Pumping in YIG/Pt Bilayers as a Function of Layer Thickness. *Phys. Rev. B: Condens. Matter Mater. Phys.* **2015**, 92 (5), 054437.
- (70) Uchida, K.; Qiu, Z.; Kikkawa, T.; Iguchi, R.; Saitoh, E. Spin Hall Magnetoresistance at High Temperatures. *Appl. Phys. Lett.* **2015**, 106 (5), 52405.